Recharacterization of RSL3 reveals that the selenoproteome is a druggable target in colorectal cancer

Stephen L. DeAngelo[1,2,11,14], Liang Zhao[2], Sofia Dziechciarz[2], Myungsun Shin[3,4], Sumeet Solanki[2], Andrii Balia[5], Marwa O El-Derany[2,6], Cristina Castillo[2], Yao Qin[7,8], Nupur K. Das[2], Hannah Noelle Bell[2], Joao A. Paulo[3,4], Yuezhong Zhang[2], Nicholas J. Rossiter[2,14], Elizabeth C. McCulla[1,14], Jianping He[9], Indrani Talukder[2], Billy Wai-Lung Ng[7,8], Zachary T. Schafer[9], Nouri Neamati[5,14], Joseph D. Mancias[4,10], Markos Koutmos[10,11,12,*], Yatrik M. Shah[2,12,13,*]

Affiliations:

[1]Doctoral Program in Cancer Biology, University of Michigan Medical School, Ann Arbor, MI, United States

[2]Department of Molecular and Integrative Physiology, University of Michigan, Ann Arbor, MI, United States

[3]Department of Cell Biology, Harvard Medical School, Boston, MA, United States

[4]Dana-Farber Cancer Institute, Boston, Massachusetts, United States

[5]Department of Medicinal Chemistry, College of Pharmacy, University of Michigan, Ann Arbor, Michigan, United States

[6]Department of Biochemistry, Faculty of Pharmacy, Ain Shams University, Cairo, Egypt.

[7]School of Pharmacy, Faculty of Medicine, The Chinese University of Hong Kong, Sha Tin, Hong Kong

[8]Li Ka Shing Institute of Health Sciences, Faculty of Medicine, The Chinese University of Hong Kong, Sha Tin, Hong Kong

[9]Department of Biological Sciences, University of Notre Dame, Notre Dame, IN, United States

[10]Division of Radiation and Genome Stability, Department of Radiation Oncology, Dana-Farber Cancer Institute, Harvard Medical School, Boston, MA. United States

[11]Department of Chemistry, University of Michigan, Ann Arbor, MI, United States

[12]Department of Biophysics, University of Michigan, Ann Arbor, MI, United States

[13]Department of Internal Medicine, University of Michigan, Ann Arbor, MI, United States

[14]Rogel Cancer Center, University of Michigan, Ann Arbor, MI, United States

*Corresponding: mkoutmos@umich.edu, shahy@umich.edu

Abstract

Ferroptosis is a non-apoptotic form of cell death resulting from the iron-dependent accumulation of lipid peroxides. Colorectal cancer (CRC) cells accumulate high levels of intracellular iron and reactive oxygen species (ROS) and are thus particularly sensitive to ferroptosis. The compound (S)-RSL3 ([1S,3R]-RSL3) is a commonly used ferroptosis inducing compound that is currently characterized as a selective inhibitor of the selenocysteine containing enzyme (selenoprotein) Gluathione Peroxidase 4 (GPx4), an enzyme that utilizes glutathione to directly detoxify lipid peroxides. However, through chemical controls utilizing the (R) stereoisomer of RSL3 ([1R,3R]-RSL3) that does not bind GPx4, combined with inducible genetic knockdowns of GPx4 in CRC cell lines, we revealed that GPx4 dependency does not always align with (S)-RSL3 sensitivity, questioning the current characterization of GPx4 as the central regulator of ferroptosis. Utilizing affinity pull-down mass spectrometry with chemically modified (S)-RSL3 probes we discovered that the effects of (S)-RSL3 extend far beyond GPx4 inhibition, revealing that (S)-RSL3 is a broad and non-selective inhibitor of selenoproteins. To further investigate the therapeutic potential of broadly disrupting the selenoproteome as a therapeutic strategy in CRC, we employed additional chemical and genetic approaches. We found that the selenoprotein inhibitor auranofin, an FDA approved gold-salt, chemically induced oxidative cell death and ferroptosis in both *in-vitro* and *in-vivo* models of CRC. Consistent with these data, we found that AlkBH8, a tRNA-selenocysteine methyltransferase required for the translation of selenoproteins, is essential for the *in-vitro* growth and xenograft survival of CRC cell lines. In summary, these findings recharacterize the mechanism of action of the most commonly used ferroptosis inducing molecule, (S)-RSL3, and reveal that broad inhibition of selenoproteins is a promising novel therapeutic angle for the treatment of CRC.

Introduction

Colorectal Cancer (CRC) is the fourth most common cancer and fifth leading cause of cancer-related deaths in the US[1]. Most early CRC is diagnosed through routine colonoscopies and if found early, CRC is curable with surgical resection and adjuvant chemotherapy[2]. However, recent data demonstrate a concerning rise in the incidence rate of CRC in young adults who often present with advanced disease[3]. Metastatic CRC is incurable and is commonly driven by inactivating mutations of the tumor suppressor genes APC and TP53, leaving minimal opportunities for the development of targeted therapeutics[4,5]. While recent advances in immunotherapy have demonstrated remarkable success in mismatch repair deficient (MMR) CRC[6], only a small subset of CRC patients are diagnosed with MMR CRC[7], limiting its widespread utility. Therefore, new effective therapies for CRC are desperately needed.

CRCs are highly addicted to iron[8–11] and thus an emerging strategy for the treatment of CRC is the induction of an iron-dependent, non-apoptotic form of cell death, ferroptosis[12]. In the presence of labile iron, intracellularly produced hydrogen peroxide undergoes radical decomposition to produce a hydroxyl radical in a process known as the Fenton reaction[13]. The hydroxyl radical rapidly proliferates through cells, leading to widespread DNA, protein, and lipid peroxidation. The accumulation of lipid peroxides is a key characteristic of ferroptosis and results in membrane instability leading to cell rupture[14]. However, in contrast to apoptosis, ferroptosis lacks distinct, well-defined markers for its characterization[15]. Therefore, the main distinguishing characteristic of ferroptosis is its ability to be rescued by the lipid reactive oxygen species (ROS) scavenging antioxidants liproxstatin-1 and ferrostatin-1[16].

Glutathione peroxidase (GPx)4 utilizes reduced glutathione (GSH) to directly detoxify lipid ROS, leading to the characterization of GPx4 as an essential regulator of ferroptosis[17]. Central to the activity of GPx4 is a catalytic selenocysteine residue as GPx4 is a selenoprotein, one of 25

82 proteins in the human genome that selectively incorporate the amino acid selenocysteine[18–20],
83 collectively known as the selenoproteome. The selenocysteine residue is often essential for
84 catalytic function as selenocysteine to cysteine point mutations in GPx4 result in >90% loss of
85 activity, albeit supraphysiological overexpression of this reduced activity mutant rescues
86 ferroptosis induction *in-vitro*[21]. The discovery of Ras-Sensitive Ligand 3 (RSL3) – identified as a
87 GPx4 inhibitor[17] – has further cemented the characterization of GPx4 as the central regulator of
88 ferroptosis[22]. While there is broad cell line sensitivity to RSL3, this does not always correlate
89 with GPx4 expression, casting doubt on RSL3 as a specific inhibitor of GPx4.
90
91 Through the generation of doxycycline-inducible GPx4 knockdown cell lines (GPx4 i-KD), we
92 identified a CRC cell line (DLD1) that is sensitive to RSL3 but insensitive to GPx4 i-KD. Next,
93 through synthesis of a biotinylated RSL3, we performed streptavidin-based affinity pulldown of
94 CRC lysates to identify RSL3 targets by tandem-mass tag (TMT) quantitative proteomics. Our
95 data revealed that RSL3 has numerous targets and is a non-specific inhibitor of the
96 selenoproteome and thioredoxin peroxidases, including the selenoprotein Thioredoxin
97 Reductase 1 (TxnRD1). Last, we employed chemical and genetic approaches to modulate the
98 selenoproteome and characterized the effects of selenoproteome inhibition on CRC cell lines. In
99 our studies we demonstrated that the selenoproteome is essential for the growth and survival of
100 CRC cell lines in *in-vitro* and *in-vivo* models, thus revealing the broad inhibition of
101 selenoproteins to be a novel therapeutic strategy in CRC.
102

103 **Methods**

104 Mice

105 All mice used in these studies are from the Balb/c, C57Bl/6J, or NOD SCID lines as indicated.
106 Males and females are equally represented, and littermates were randomly mixed in all
107 experimental conditions. The mice were housed in a temperature controlled, specific pathogen
108 free environment, with a 12-hour light/dark cycle. They were fed *ad-libitum* with either a
109 standard chow diet or auranofin dosed diet as indicated. Mice were between 6 and 8 weeks old
110 at study initiation. All animal studies were carried out in accordance with the Association for
111 Assessment and Accreditation of Laboratory Animal Care International guidelines and approved
112 by the University Committee on the Use and Care of Animals at the University of Michigan.

113

114 Xenograft studies

115 CT26 cells were maintained for 2 weeks at < 70% confluency prior to injection into fully immune-
116 competent Balb/c mice. Prior to injection, cells were trypsinized, thoroughly washed, and
117 resuspended in sterile saline to a final injection volume of 100 µL. Wild-type mice of both sexes
118 were anesthetized via inhaled isoflurane (induction dose 3-4%, maintenance dose 1-2%) and
119 inoculated with 0.4×10^6 CT26 cells. Cells were implanted into lower flanks and treatment
120 began on day 4 once palpable tumors were identified. Tumor size was measured with digital
121 calipers utilizing the formula $V=0.5*L*W^2$. Xenograft treatments used in this study included the
122 following: auranofin injection (10mg/kg, IP, daily), auranofin chow (1.25-10mg/kg, *ad libitum*),
123 doxycycline chow (400 mg/kg, *ad libitum*), NAC drinking water (20mM, *ad libitum*)

124

125 Ethical endpoints for xenograft studies were determined in accordance with Association for
126 Assessment and Accreditation of Laboratory Animal Care International guidelines and approved
127 by the University Committee on the Use and Care of Animals at the University of Michigan.
128 Ethical endpoints for this study were determined to be any of the following: 30 days post

129 implantation, tumor size exceeding 2 cm in any direction, hemorrhage of the tumor, or
130 indications of tumor induced pain and decreased mobility. Once endpoint was determined for
131 any of the groups, all mice in study were euthanized by CO_2 inhalation and tumors were
132 excised. Tumor volume and weight were measured, and tissues were prepared for histology,
133 IHC, or flow cytometry as indicated. A licensed veterinarian was available for consult at all
134 points during the study.
135
136 AOM/DSS induction of colitis-associated colorectal cancer
137 C57BL/6J mice were utilized to model colitis-associated colon cancer as previously
138 described[10,23,24].
139
140 Briefly, at 6 weeks of age mice were weighed and injected intraperitoneally with 10 mg/kg of
141 Azoxymethane (AOM). Three days following AOM injection mice began their first cycle of 2%
142 (w/v) Dextran Sodium Sulfate (DSS) water. Following a DSS cycle, mice began a 14-day
143 recovery period before the next cycle of DSS treatment. Treatment with Auranofin chow began
144 7 days following the conclusion of the 3rd administration of DSS water and continued for 30
145 days. At the conclusion of the study all mice were euthanized, and the colons were extracted for
146 analysis. Histological analysis was performed via a study-blinded independent pathologist.
147
148 Human Survival Analysis
149 Human survival analysis was determined using the online tool KMplot[25]. This is a web-based,
150 registration-free survival analysis tool that can perform univariate and multivariate survival
151 analysis. Significance is computed using the Cox-Mantel log-rank test.
152
153 Human Normal vs Tumor Gene Expression Analysis
154 Human normal vs. tumor gene expression analysis was determined using the online tool

155 UALCAN (University of Alabama at Birmingham Cancer Data Analysis Portal)[26,27]. This is a
156 web-based, registration-free gene expression analysis tool for the analysis of cancer OMICS
157 data from the TCGA (The Cancer Genome Atlas Project).
158
159 Cell lines
160 Human CRC cell lines HCT116, RKO, SW480, and DLD1, and the mouse CRC cell line CT26
161 were used. Cell lines have been STR-authenticated and routinely tested for mycoplasma
162 contamination by PCR. All cells were maintained in complete DMEM medium (supplemented
163 with 10% fetal bovine serum (Cytiva) and 1% antibiotic/antimycotic agent (Thermo Fisher)) at 37
164 °C in 5% CO_2 and 21% O_2. Cell numbers were quantified for plating and xenograft experiments
165 using a Multisizer 4e Coulter Counter (Beckman-Coulter).
166
167 Growth assays
168 Adherent cell growth assays were performed via label free live cell imaging using the Cytation 5
169 Imaging Multi-Mode reader with attached BioSpa (Agilent BioTek). For 72 hr growth analysis
170 cells were plated at ~500 cells/well while for 144 hr growth analysis cells were plated at ~100
171 cells/well. Cells were allowed to adhere overnight, imaged and analyzed for cell number at t_0,
172 and then immediately treated as indicated in the figure legend; images were then acquired
173 every 8-24 hr as indicated. Cytation software was used to quantify adherent cell counts.
174 Analysis was performed by normalization to cell number at first reading (0 hr), with a minimum
175 of 3 independent wells averaged for statistical analysis. Graphs were plotted using Prism with
176 error bars representing mean +/- standard deviation. Growth assay data was utilized for the
177 generation and calculation of EC_{50} curves. The average fold change at the endpoint of an
178 untreated control group (minimum of 3 replicates) was normalized to a value of 1.0 and the
179 relative fold change of treated wells (minimum 3 replicates per group) was then calculated as a
180 fractional response as compared to the average of the untreated control. EC_{50} values were

181 determined using Prism sigmoidal standard curve interpolation. Statistical significance was
182 determined using Prism 2-way ANOVA with multiple comparisons.
183
184 Clonogenic Assays (Colony Formation Assays)
185 Cells were plated in biological triplicates in a 6-well plate at 500 cells per well in 3 mL of media.
186 Cells were treated as indicated in the figure legends with media and treatment replenished
187 every 5 days. Assays were concluded at 12-15 days by fixing cells in cold 10% buffered formalin
188 for 10 min and staining with 1% crystal violet, and 10% methanol solution for 30 min. Colony
189 plates were washed in dH_2O and imaged using an iBright FL1500 imaging system (Thermo
190 Fisher)
191
192 Histological Staining
193 Colonic tissues or tumor tissues were rolled and fixed with PBS-buffered formalin for 24 hours
194 then transferred to 70% ethanol, followed by embedding in paraffin. Sections of 5 μm were
195 stained for H&E and mounted with Permount Mounting Medium (Thermo Fisher Scientific).
196
197 Western Blotting
198 Indicated cells were seeded in a 6-well plate in triplicate for each condition and allowed to
199 adhere overnight. Cells were plated to reach ~$0.8x10^6$ cells/well at time of harvest. Cells were
200 lysed with RIPA assay buffer with added protease (1:100 dilution; MilliporeSigma) and
201 phosphatase (1:100 dilution; Thermo Fisher Scientific) inhibitors. Lysates were quantified by
202 BCA protein assay kit (Pierce – Thermo Fisher Scientific) and normalized for loading.
203 Solubilized proteins were resolved on 10% SDS-polyacrylamide gels and transferred to
204 nitrocellulose membrane, blocked with 5% milk in TBST, and immunoblotted with the indicated
205 primary antibodies: GPx4 monoclonal (Proteintech 67763-1-Ig), TxnRD1 (Santa Cruz sc-
206 28321), Actin (Proteintech 66009-1-Ig). HRP-conjugated secondary antibodies used were anti-

207 rabbit and anti-mouse at a dilution of 1:2000 and immunoblots were developed using Chemidoc
208 imaging system (ChemiDoc, BioRad).
209

210 CETSA Assay

211 293T cells cultured in 10 cm dishes were treated with 10 μM compound (1R,3R-RSL3, 1S,3R-
212 RSL3, Auranofin) or DMSO control (0.1%, v/v) for 1 hour at 37 °C. After treatment, cells were
213 harvested and the cell suspensions in PBS were distributed into 12 PCR tubes and heated to
214 indicated temperatures (43.0, 43.5, 45.7, 48.9, 52.4, 55.9, 57.4, 60.5, 63.3, 65.6, 66.3, and
215 66.7°C) for 3 minutes. After cooled to room temperature for an additional 3 min, cells were lysed
216 by liquid nitrogen with freeze and thaw cycles. Samples were supplemented with protease
217 inhibitor cocktail (#HY-K0010, MCE). Subsequently, the cell lysates were centrifuged at 20,000 g
218 at 4 °C for 20 minutes. The supernatant was carefully collected and diluted with 5× SDS loading
219 buffer (#AIWB0025, Affinibody) for SDS–PAGE (#ET15420LGel, ACE) and western blotting
220 analysis.

221

222 qPCR

223 Cell lines were treated for indicated times (typically 72 hrs) and washed with sterile PBS prior to
224 RNA extraction with Trizol reagent. Total RNA was visualized on an agarose gel to confirm high
225 quality extraction, with RNA yield quantified using a Nanodrop. 1μg of total RNA was reverse
226 transcribed to cDNA using SuperScriptTM III First-Strand Synthesis System (Invitrogen). Real
227 time PCR reactions were set up in three technical replicates for each sample. cDNA gene
228 specific primers and SYBR green master mix were combined and then run in QuantStudio 5
229 Real-Time PCR System (Applied BioSystems). The fold-change of the genes were calculated
230 using the ΔΔCt method using *Actb* as the housekeeping mRNA. qPCR primers used:
231 Actin F: CACCATTGGCAATGAGCGGTTC. Actin R: AGGTCTTTGCGGATGTCCACGT

232 AlkBH8 F: AGGTCTTTGCGGATGTCCACGT AlkBH8 R: GAGAGCATCCACCAGTCCACAT

233

234 Generation of Doxycycline Inducible Cell Lines

235 Doxycycline inducible cell lines were generated using the pLKO.1-Tet On system[28]. shRNA
236 sequences were cloned into the pLKO.1-Tet On backbone, sequence validated via Sanger
237 Sequencing (Genscript), and utilized for lentivirus production through the University of Michigan
238 Vector Core. Cells were transfected with lentiviral particles through spinfection at 900xg, 37 °C,
239 1 hr in the presence of polybrene (final concentration = 10 µg/mL) then incubated at 37 °C, 5%
240 CO2 for 24 hrs. The next day media was changed and cells were allowed to recover for 24 hrs
241 before addition of puromycin (2 µg/mL) to the culture media. Cells were maintained in
242 puromycin until an untreated control well demonstrated 100% cell death. shRNA sequences:
243 GPx4 sh2: GTGGATGAAGATCCAACCCAA
244 GPx4 sh3: GCACATGGTTAACCTGGACAA
245 AlkBH8 sh3: TTACCTGAACACATCATATAT
246 AlkBH8 sh4: CAGGTGGGAAGGCACTCATTT

247

248 Streptavidin-Affinity Pull Down

249 Streptavidin-Affinity MS was performed on isolated cell lysates. Cells were plated in 15 cm
250 dishes in normal DMEM (10% FBS, 1% Anti-Anti) and allowed to adhere for 24 hrs. The next
251 day cells were treated with 1 µM selenium in the form of Sodium selenite to increase translation
252 of trace selenoproteins that may otherwise be vulnerable to dropout. Sodium selenite was
253 prepared as a 100 mM stock in ddH_2O. 24 hrs after administration of selenium, cells were
254 washed with sterile PBS and scraped directly into ice cold RIPA buffer. The protocol was
255 optimized to utilize 10 mg of total lysate per biological replicate to obtain signal over the noise
256 threshold. Soluble lysate was treated overnight at 4 °C with the EC_{50} concentration of the
257 respective compound. The next day Streptavidin-coated magnetic beads (Vector Laboratories)

258 were added and the mixture was incubated with gentle rocking at 4 °C for 2 hrs. Beads were
259 then washed 3x in RIPA using a magnetic separation rack, and a further 3x in SDS-free wash
260 buffer (50 mM Tris-HCl, pH 7.4, 150 mM NaCl, 1 mM TCEP). Beads were then pelleted via
261 centrifugation, flash frozen in LN_2, and stored at -80 °C prior to MS processing.
262
263 LC-MS/MS
264 All samples were resuspended in 100 mM 4-(2-Hydroxyethyl)-1-piperazinepropanesulfonic acid
265 (EPPS) buffer, pH 8.5, and digested at 37 °C with trypsin overnight. The samples were labeled
266 with TMT Pro and quenched with hydroxylamine. Samples were desalted via StageTip and
267 dried with speedvac. Samples were resuspended in 5% formic acid, and 5% acetonitrile for LC-
268 MS/MS analysis. Mass spectrometry data were collected using an Astral mass spectrometer
269 (Thermo Fisher Scientific) coupled with a Vanquish Neo liquid chromatograph (Thermo Fisher
270 Scientific) with a 75 min gradient and Nano capillary column (100 µm D) packed with ~35 cm of
271 Accucore C18 resin (Thermo Fisher Scientific). A FAIMSPro (Thermo Fisher Scientific) was
272 utilized with -30,-35,-45,-55,-60, and -70V for field asymmetric waveform ion mobility
273 spectrometry (FAIMS) ion separations. Data acquisition was performed with a mass range of
274 m/z 350-1350 using a TopSpeed method of 1 s. MS1 resolution was set at 60,000 and singly-
275 charged ions were not sequenced. MS1 AGC target was set as standard, and the maximum ion
276 time was set at 50 ms. For MS2 analysis in the Astral analyzer, only multi-charge state ions
277 (z=2-5) were isolated and fragmented using an HCD collision energy of 35%, an isolation
278 window of 0.5 Th, with a dynamic exclusion of 15 s. MS2 AGC target was set as standard, and
279 the maximum ion time was set at 20ms.
280
281 Raw files were searched using the Comet algorithm with a custom database search engine
282 reported previously[29]. Database searching included human (*Homo Sapiens*) entries from
283 UniProt (http://www.uniprot.org, downloaded 2021) with the reversed sequences, and common

284 contaminants (i.e., keratins, trypsin). Peptides were searched using the following parameters:
285 50 ppm precursor mass tolerance; up to 2 missed cleavages; variable modifications: oxidation
286 of methionine (+15.9949); static modifications: TMTpro (+304.2071) on lysine and peptide N-
287 terminus, carboxyamidomethylation (+57.0215) on cysteines and selenocysteines. The protein-
288 level FDR was determined using the ModScore algorithm where a score of 13 corresponds to
289 95% confidence in correct localization. TMT reporter ions were used for quantification of peptide
290 abundance. Isotopic impurities were corrected according to the manufacturer's specifications,
291 and signal-to-noise (S/N) was calculated. Peptides with summed S/N lower than 100 across all
292 channels or isolation specificity lower than 0.5 were discarded. The high confidence peptides
293 were then used to quantify protein abundance by summing up S/N values for all peptides
294 assigned to the same protein, and only proteins in the linear quantification range of the
295 instrument were included in the analysis. The normalization for protein quantification was then
296 performed by adjusting protein loadings of total sum of S/N values to that of every TMT channel.

297 Statistical Overrepresentation Test

298 Statistical overrepresentation analysis/test of proteins pulled down with Biotin-(1S,3R)-RSL3
299 was performed on the portion of the hit list that met all the following criteria: 1) >1 peptide
300 identified by TMT-MS, 2) p-value < 0.050, 3) fold enrichment > 2. This list of genes was then
301 input into PANTHER database (v18.0) and analyzed for protein class overrepresentation. As
302 selenoproteins are not annotated as a protein class in this current version of PANTHER, we
303 calculated the probability of observing a selenoprotein in a random set of genes from the human
304 genome as 25/20592 (utilizing the reference list size of PANTHER v18.0). This probability value
305 was scaled to our input list and a Fisher's exact t-test was performed for statistical significance.
306

307 C11-BODIPY lipid ROS measurement

308 Indicated cells were seeded in 12-well plates and allowed to adhere overnight at 37 °C prior to

309 beginning the indicated treatment or targeted gene knockdown induced by doxycycline. Cells
310 were harvested using PBS-EDTA (5 mM), buffer, washed once with HBSS, suspended in HBSS
311 containing 5 μM C11-BODIPY (Thermo Fisher), and incubated at 37 °C for 30 min. Cells were
312 pelleted, washed, and resuspended in HBSS. Fluorescence intensity was measured on the
313 FITC channel using the Beckman Coulter MoFlo Astrios. A minimum of 20,000 cells were
314 analyzed per condition. Data were analyzed using FlowJo software (Tree Star). Values are
315 expressed as MFI.
316
317 Synergy Calculations
318 Synergy was calculated through disproof of the null hypothesis that treatment with two
319 biologically active compounds would produce a result in line with the Bliss Model of
320 Independence as previously described[30].
321
322 ICP-MS
323 Whole blood from indicated mice were obtained via submandibular vein puncture or from the
324 orbital sinus. Whole blood was collected in untreated sterile 1.5 mL Eppendorf tubes and
325 allowed to coagulate for 1-2 hrs at RT. Coagulated samples were spun at 13,000xg for 15 min
326 and serum was collected. Collected serum was further clarified with a second spin at 13,000xg
327 for 15min. 10 μL of clarified serum was treated with 2 mL/g total wet weight nitric acid (20 μL)
328 (Trace metal grade; Fisher) for 24 hr, and then digested with 1 mL/g total wet weight hydrogen
329 peroxide (10 μL) (Trace metal grade; Fisher) for 24 h at room temperature. The samples were
330 preserved at 4 °C until quantification of metals. Ultrapure water (VWR Chemicals
331 ARISTAR®ULTRA) was used for final sample dilution to 3 mL. Samples were then analyzed
332 using inductively coupled plasma mass spectrometry (ICP-MS) (Perkin Elmer) utilizing Bismuth
333 as an internal standard.
334

335 Auranofin Diet

336 Auranofin diet was made from powdered laboratory rodent diet (LabDiet) mixed with appropriate
337 quantities of drug in a KitchenAid mixer designated for laboratory use. Diet dosing was
338 calculating assuming an average mouse weight of 25 g and chow consumption of 4 g/day as
339 previously published[31]. Water was added to a hydration level of 60% (600 mL H_2O per kg of
340 diet) and thoroughly mixed. Small quantities of food-grade coloring (McCormick) were added to
341 differentiate doses of diet. Following mixing, the diet was extruded into pellets and dehydrated
342 for 72 hr with a food dehydrator at 41 °C (Nesco). Mice were not provided an alternate food
343 source when undergoing treatment and weight was routinely monitored.

344

345 Thioredoxin Reductase Activity Assay

346 Thioredoxin Reductase (TxnRD) activity assay was based on the plate reader procedure as
347 outlined by Cunnif *et al.*, Anal. Biochem, 2013[32] and established by Arnèr *et al.*, Methods in
348 Enzymology, 1999[33]. Briefly, the TxnRD activity assay is based on consumption of the
349 diselenide amino acid selenocystine in cell lysate, measured by NADPH consumption via
350 absorbance at 340 nm on a spectrophotometric plate reader (Cytation 5, BioTek). TxnRD is the
351 only cellular enzyme capable of reducing selenocystine, consuming NADPH in the process. A
352 master-mix of 2 mM NADPH and 1 mM selenocystine was prepared fresh for each assay.
353 NADPH (Sigma Aldrich) solution was prepared in 100 mM Tris, pH 8; fresh solution was used
354 whenever possible and solution was used within 1 week if frozen at -20 °C, with reduced initial
355 absorbance observed when utilizing thawed NADPH. As selenocystine does not readily dissolve
356 in aqueous buffer, selenocystine (Cayman Chemical Company) was first dissolved in 1N NaOH
357 (650 µL for a 50 mg vial), to which ½ volume of 1N HCl was added to neutralize the solution.
358 The master stock was then diluted to 45 mM in ddH2O and stored at -20 °C. Cells were plated
359 and treated as indicated, washed in PBS, and lysed in RIPA buffer. The insoluble fraction was
360 removed via centrifugation (13,000xg, 10 min, 4 °C) and protein abundance was quantified by

361 BCA Protein Assay (Thermo Scientific). 50 µg of protein was utilized per well in a total volume of
362 60 µL, to which 40 µL of NADPH/Selenocystine master-mix was added. Immediately following
363 addition of the master-mix (within 2 min), kinetic reading of absorbance values was initiated,
364 with reads taken every 60 s for 30 min.
365
366 CRISPR Co-Essentiality Network Generation
367 CRISPR gene effect scores from the DepMap 22Q2 release were first corrected using Cholesky
368 whitening as previously described[34]. A matrix of p-values corresponding to gene-wise Pearson
369 correlations was calculated from the whitened data, then converted to FDR values using the
370 p.adjust() function in R. A network was then constructed from all partners within 2 edge
371 distances from a given gene of interest, using an FDR cutoff of 0.05 to define
372 edges/partnership. Network graphs were generated from pairwise gene lists using the tidygraph
373 and ggraph packages in R, with the layout argument in ggraph set to "graphopt"
374
375 AGB 364/366 synthesis
376 **Scheme 1. Synthesis of Cpd24 and Biotinylated Analog[a]**

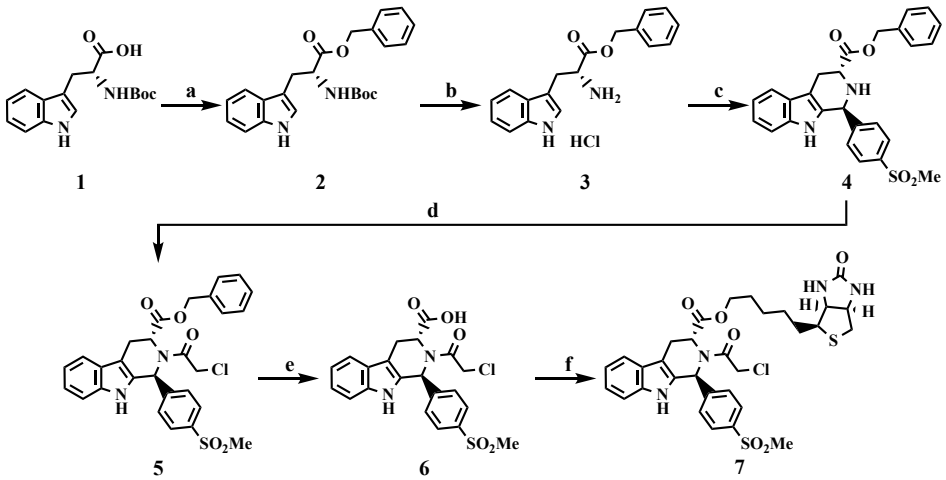

377

[a]Reagents and conditions: (a) BnOH, EDC, DMAP, THF, rt, overnight; (b) 4 N HCl in 1,4-dioxane, rt, overnight, 92% over 2 steps; (c) 4-(methylsulfonyl)benzaldehyde, IPA, reflux, 87%; (d) $ClCH_2C(O)Cl$, TEA, CH_3CN, reflux, 87%; (e) H_2, Pd/C, EtOH, rt, overnight, 72%; (f) *D*-biotinol, EDC, DMAP, THF, rt, overnight, 4%.

Scheme 2. Synthesis of RSL3 and Biotinylated Analog[b]

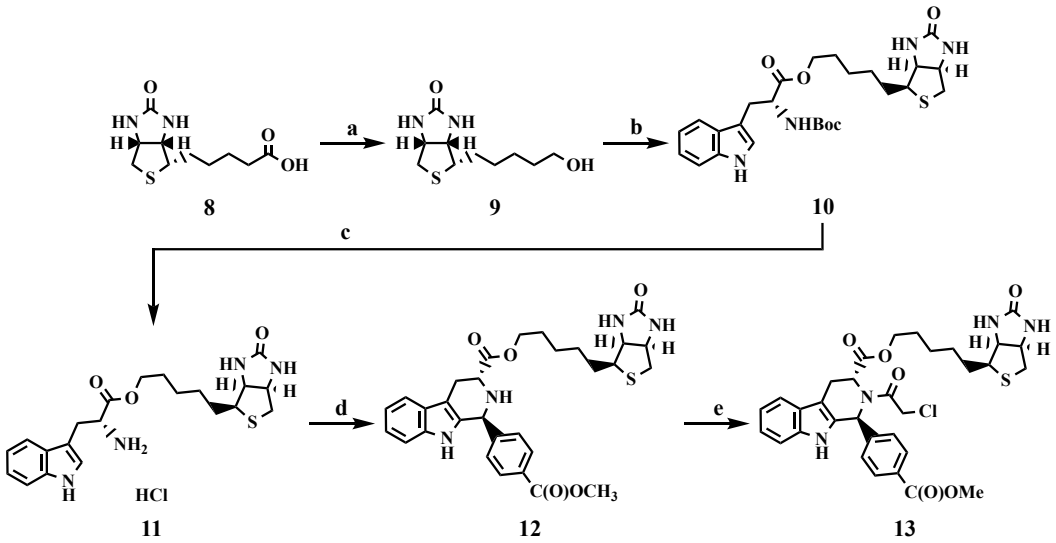

[b]Reagents and conditions: (a) $LiAlH_4$, THF, reflux, overnight, 45%; (b) (*tert*-butoxycarbonyl)-*D*-tryptophan, EDC, DMAP, THF, rt, overnight, 74%; (c) 4 N HCl in 1,4-dioxane, rt, overnight, 91%; (d) methyl 4-formylbenzoate, IPA, reflux, 15%; (e) $ClCH_2C(O)Cl$, TEA, CH_3CN, reflux, 19%.

Statistics

Data are represented as mean ± standard deviation. unless otherwise indicated. Data are from a minimum of 3 independent experiments measured in triplicate unless otherwise stated in the figure legend. For statistical analyses, unpaired *t*-tests were conducted to assess the differences between 2 groups. One-way or 2-way ANOVA was used for multiple treatment conditions followed by Tukey's post hoc test. A strict p-value cutoff of < 0.050 was utilized for determination of significance in all experiments. All statistical tests were carried out using Prism 10 software (GraphPad).

395

396 Study approval

397 All animal studies were carried out in accordance with Institute of Laboratory Animal Resources

398 guidelines and approved by the University Committee on the Use and Care of Animals at the

399 University of Michigan (IACUC protocol number: PRO00011805)

400

401 **Results**

402 **The potency of (S)-RSL3 is due to GPx4 independent effects in CRC cell lines.**

403 The most commonly utilized mechanism of ferroptotic induction is treatment with the small
404 molecule GPx4 inhibitor RSL3 (Figure 1A). RSL3 has two stereoisomers, (1S,3R)-RSL3 and
405 (1R,3R)-RSL3, which we will refer to as (S) and (R)-RSL3, respectively (Figure 1B). The (S) and
406 (R) stereoisomers of RSL3 differentially target GPx4[22] (Figure 1C, S1A), with the ability of (S)-
407 RSL3 to more potently inhibit GPx4 hypothesized to directly correlate with its increased potency.
408 Utilizing 72 hr live cell imaging growth assays we confirmed that (S)-RSL3 is markedly more
409 potent than (R)-RSL3 in the HT1080 fibrosarcoma cell line that is frequently utilized in
410 ferroptosis research[35]. The EC_{50} values of 13 nM for (S)-RSL3 and 903 nM for (R)-RSL3 (Figure
411 1D-E) are consistent with previously reported cell death and viability measurements[17]. However,
412 both (S)-RSL3 and (R)-RSL3 exhibited nearly equipotent sensitivity in CRC cell lines DLD1,
413 HCT116, RKO, and SW480, with EC_{50} values at ~1 μM (Figure 1F). Notably, DLD1 cells
414 displayed a 2-fold increased sensitivity to (R)-RSL3, despite the decreased affinity of (R)-RSL3
415 towards GPx4.

416

417 In contrast to other forms of regulated cell death, ferroptosis lacks specific cellular markers and
418 is instead assessed through the ability to rescue cell death with lipid-ROS scavenging agents
419 such as Liproxstatin-1 (Lip-1)[16]. In our growth assays, we aimed to delineate the "ferroptotic
420 window" induced by (S) and (R)-RSL3 through Lip-1 co-treatment. Despite broad cell line
421 sensitivity to (S)-RSL3, the ferroptotic window varied significantly between cell lines and often
422 did not result in a complete rescue of (S)-RSL3 treatment (Figure 1G, S1B). In agreement with
423 previous data, (R)-RSL3 decreased cell growth, which was not rescued by Lip-1 at any dose in
424 our cell line panel (Figure 1H, S1C). The equipotent nature of these two compounds suggest
425 that while GPx4 inhibition likely drives ferroptosis, the potency of (S)-RSL3 in CRC cell lines
426 may be driven by a GPx4-independent activity.

427 **RSL3 sensitivity does not predict GPx4 essentiality in CRC cell lines**

428 To investigate if (S)-RSL3 functions independently of its ability to inhibit GPx4 in CRC, we
429 generated stable cell lines with doxycycline-inducible GPx4 shRNAs (GPx4 i-KD). Two RNA
430 guides for GPx4, sh2 and sh3, were found to decrease GPx4 levels by >95% at 72 hr post
431 doxycycline treatment (Figure 2A, S2A). GPx4 was confirmed to be essential for cell growth in
432 the CRC cell lines SW480, RKO, and HCT116, however DLD1 cells were insensitive to GPx4 i-
433 KD despite sensitivity to (S)-RSL3 (Figure 2B). Furthermore, near complete GPx4 i-KD in DLD1
434 cells resulted in a 10-fold increase in sensitivity to (S)-RSL3 (Figure 2C), supporting the
435 hypothesis that the potency of (S)-RSL3 in CRC cells can be due to GPx4-independent effects.
436 We additionally tested a next generation GPx4 inhibitor, the ML210[36] derivative JKE1674[37].
437 JKE1674 is markedly less potent than (S)-RSL3 across CRC cell lines and is inactive up to 20
438 μM in the DLD1 cell line (Figure 2D). JKE1674 exhibited significantly lower potency in CRC lines
439 as compared to (S)-RSL3, and the decreases in growth induced by JKE1674 treatment up to 20
440 μM were completely rescued by Lip-1, as demonstrated in the RKO cell line (Figure 2E).
441

442 Altogether, these data demonstrate that the DLD1 cell line is insensitive to modulation of GPx4
443 activity despite sensitivity to (S)-RSL3. Recent data have suggested that a target of (S)-RSL3 is
444 the selenoprotein Thioredoxin Reductase (TxnRD1)[38], which regulates the activity of thioredoxin
445 peroxidases, also known as peroxiredoxins (PRDXs) [39,40](Figure S2B). Utilizing an in-house
446 thioredoxin reductase activity assay we confirm that (S)-RSL3 also potently inhibits TxnRD
447 activity. Interestingly, DLD1 cells had the highest TxnRD activity across tested CRC lines
448 (Figure S2C-E).

449 **Chloroacetamide-based ferroptosis inducers non-selectively inhibit the selenoproteome**

450 To determine the targets of (S)-RSL3 in CRC cells we synthesized a biotinylated derivative,
451 utilizing the same attachment site at the 3 position as the original fluorescein conjugate utilized
452 for chemoproteomics in 2014[17] (Figure 3A). The synthesis yielded a small quantity of
453 biotinylated (R)-RSL3 which we used to validate that the biotin group did not significantly alter
454 the potency of these compounds (Figure 3B). Following optimization of pull-down protocol,
455 including 1 μM selenium supplementation to increase trace selenoprotein expression (Figure
456 S3A), streptavidin-based pull-downs of (S)-RSL3 vs biotin-(S)-RSL3 were performed on
457 biological triplicates. The use of Tandem Mass Tag (TMT) labeling combined with the use of
458 next-generation mass spectrometers has offered unparalleled sensitivity, revealing that while
459 (S)-RSL3 does inhibit GPx4, it is also a broadly non-specific inhibitor (Figure 3C). However, we
460 suspect that many of these targets may not be pharmacologically relevant, as the
461 chloroacetamide moiety utilized in the RSL3 "warhead" is known to be highly reactive and
462 broadly non-specific[41]. To further explore the targets of chloroacetamide-based ferroptosis
463 inducers we synthesized a biotinylated version of the RSL3 derivative Cpd24[42], observing near
464 identical results to biotinylated (S)-RSL3 (Figure S3B). Statistical overrepresentation analysis
465 revealed two heavily enriched protein classes as targets of (S)-RSL3, peroxidases and
466 selenoproteins (Figure 3D-E).

467

468 **Gold therapy inhibits the selenoproteome and can induce *in-vitro* ferroptosis in CRC**

469 Our data suggests that in addition to its ability to inhibit GPx4 and TxnRD1 – disrupting both
470 cellular mechanisms of peroxide detoxification (Figure 4A) – the potency of (S)-RSL3 may also
471 arise from its ability to broadly inhibit the selenoproteome. We hypothesized that alternative
472 strategies of non-specific selenoprotein inhibition may also be capable of inducing oxidative
473 stress and ferroptosis in CRC cells. To test this hypothesis we used the gold salt containing
474 small molecule auranofin, as ionic gold potently forms Au-Se inhibitory adducts[43,44]. Auranofin is

475 primarily characterized as a TxnRD1 inhibitor[45,46] with the ability to non-specifically inhibit other
476 selenoproteins[47–49]. However, all small molecules have intrinsic bias in their protein targets and
477 in our hands by CETSA analysis, auranofin showed no statistically significant interaction with
478 GPx4 (Figure S4A-B), providing a unique opportunity to study broad disruption of the
479 selenoproteome without the dominant effects of GPx4 inhibition in these ferroptosis sensitive
480 cell lines.
481
482 To investigate the therapeutic potential of alternative selenoprotein inhibition strategies in CRC
483 we initially performed dose response curves across our CRC cell line panel, observing that CRC
484 cells display broad and potent sensitivity to auranofin. Furthermore, several cell lines (RKO,
485 SW480) displayed statistically significant rescue of auranofin treatment by Lip-1 (Figure 4B),
486 demonstrating that gold-based inhibition of the selenoproteome can induce ferroptosis (in a
487 dose and cell line specific manner).
488
489 We next sought to further characterize the mechanism of auranofin based growth inhibition, as
490 auranofin is a potent inducer of apoptosis in other cell lines[50]. Supporting a primary role of
491 selenoproteins as antioxidant enzymes, all tested concentrations of auranofin were rescued by
492 the general antioxidant N-Acetyl Cysteine (NAC) while the apoptosis inhibitor Z-Vad-FMK[51,52] or
493 the necroptosis inhibitor Nec-1[53] (Figure 4C) induced a slight cell line specific rescue. Therefore,
494 mechanisms of growth inhibition outside of ferroptosis induced by selenoprotein inhibitors
495 appear to also be both dose and cell line dependent. However, when inhibitor concentrations
496 are increased to the μM range, growth can no longer be rescued with any specific cell death
497 inhibitor, supporting a hypothesis that high doses of auranofin induce non-specific oxidative
498 necrosis, consistent with our observations for (S)-RSL3.
499
500 To more fully recapitulate the proposed mechanism of (S)-RSL3, the potency of auranofin was

501 tested in combination with GPx4 KD. As we have previously demonstrated, the DLD1 shGPx4-2
502 cell line is insensitive to GPx4 i-KD, yet combination with GPx4 KD synergistically increased the
503 potency of auranofin treatment (Figure 4F). This combination also drastically shifted the primary
504 mechanism of lower dose auranofin treatment to ferroptosis as determined by Lip-1 rescue
505 (Figure 4E). Altogether these data support a model where (S)-RSL3 activity is driven by its
506 ability to function as a pan-inhibitor of the selenoproteome to broadly inhibit cellular antioxidant
507 systems.
508
509 **Gold therapy reduces CRC growth *in-vivo***
510 We next sought to validate our *in-vitro* findings in an *in-vivo* setting. For these studies, we
511 utilized the CT26 cell line, a mouse derived colorectal adenocarcinoma cell line suitable for
512 growth in fully immunocompetent Balb/c mice. After confirmation that CT26 cells were
513 responsive to auranofin treatment, Lip-1 rescue demonstrated that CT26 cells possess a large
514 and potentially targetable ferroptotic window where doses of auranofin between 60nM and 2μM
515 can be significantly rescued with Lip-1 (Figure 5A). Following flank implantation of 0.4×10^6
516 CT26 cells per mouse, treatment with auranofin (10 mg/kg, IP, daily) began once tumors were
517 palpable at day 4. At the primary study endpoint (tumor size >2 cm in any direction within a
518 control mouse), IP-treated mice displayed a consistent ~30% reduction in final tumor mass
519 (Figure 5B), with histological staining demonstrating signs of intra-tumoral necrosis (Figure 5C).
520 However, daily IP of auranofin was not well tolerated as treated mice displayed weight loss and
521 increased stress on handling. As auranofin is orally bioavailable, custom rodent chow was made
522 in-house in a range of concentrations providing dosing from 1.25-10 mg/kg based on an
523 average daily consumption of 4g chow per mouse per day[31]. Additionally, as auranofin rapidly
524 dissociates in plasma to release ionic gold, the bioavailability of auranofin administration can be
525 estimated through analysis of serum gold concentration using inductively coupled plasma mass
526 spectrometry (ICP-MS). Dose optimization studies on non-tumor bearing mice demonstrate that

527 diet administration of auranofin allows for an accurate and reproducible *in-vivo* dose response,
528 with identical endpoint plasma gold concentrations observed between 10 mg/kg administration
529 by chow or IP (Figure S5A). Dose optimization studies also demonstrated that auranofin
530 administration via chow was much better tolerated than IP administration (Figure S5B).
531 Furthermore, ICP-MS data demonstrated that mice administered 10 mg/kg auranofin display
532 plasma gold levels equivalent to patients receiving 6 mg/day auranofin[54,55] (0.5-0.7 μg/mL),
533 estimated at plasma concentrations equivalent to ~1-2 μM auranofin[56].
534
535 We next repeated our CT26 xenograft study with our in-house formulated dose response chow.
536 Doses of 2.5mg/kg and 10mg/kg were chosen to test effects of both low and high dose
537 auranofin in this tumor model. Interestingly, we observed equal effects in tumor growth
538 reduction at both tested doses, which were fully rescuable with co-administration of NAC in
539 drinking water (Figure 5D). Flow cytometry analysis of auranofin-treated tumors confirmed
540 differential *in-vivo* mechanisms, with only low dose auranofin chow capable of increasing intra-
541 tumoral lipid-ROS (Figure 5E).
542
543 However, CRC has a unique microenvironment in the colon that is not recapitulated in a flank
544 xenograft model. Therefore, we aimed to use the AOM/DSS model of chemical carcinogen-
545 induced colorectal cancer to study the effects of auranofin on a diverse population of cells within
546 the native microenvironment (Figure 5F). We chose to use 2.5 mg/kg auranofin chow for this
547 study as it was the lowest effective dose in flank xenograft studies. Furthermore, as 2.5 mg/kg
548 auranofin chow was observed to induce lipid-ROS in our flank tumors, this dose allowed us to
549 study the effects of *in-vivo* induction of ferroptosis on CRC tumor progression. Mice were
550 administered a single injection of AOM intraperitoneally followed by three 7-day cycles of DSS
551 with a two-week recovery period between cycles. Following the last cycle of DSS, mice were

552 given a brief recovery period of 7 days and then administered auranofin chow *ad-libitum* until
553 study endpoint. Mice were euthanized after 30 days on auranofin chow. Total number of tumors
554 per mouse trended lower in the treated mice, there was a significant reduction in tumor size and
555 total tumor burden in the auranofin treated group (Figure 5G). While control mice often had
556 large, vascularized colon tumors, the tumors of the auranofin treated group failed to progress
557 (Figure 5H). Histological analysis further confirmed the presence of multiple areas of neoplasia
558 in both groups (Figure 5I), with the tumors of the control group significantly larger than those in
559 the treated group.
560
561 **The tRNA-Sec methyltransferase AlkBH8 is required for CRC growth *in-vitro***
562 To confirm that general inhibition of the selenoproteome is an efficacious target for therapeutic
563 intervention in CRC, a genetic approach to modulate the selenoproteome was required. To
564 guide our approach, co-essentiality analysis revealed that Gpx4 and TxnRD1 are co-essential
565 with the bulk of the tRNA-sec biosynthetic pathway (Figure S6A-B). From these analyses, we
566 identified the tRNA-methyltransferase AlkBH8 as a potential novel therapeutic target in CRC, as
567 increased AlkBH8 expression most significantly correlates with decreased overall survival in
568 CRC patients (Hazard Ratio = 1.6, p = 0.034) as compared to other members of the tRNA-sec
569 biosynthetic pathway (Figure 6A, S6C). AlkBH8 has been extensively reported to regulate the
570 selenoproteome via methylation of tRNA-selenocysteine, with AlkBH8 knockdown and knockout
571 models demonstrating a decreased ability to translate selenoproteins[57–64]. From analysis of
572 TCGA banked tumor samples we observed that AlkBH8 expression is significantly increased in
573 primary tumor samples as compared to normal controls (Figure 6B), and that patients with early-
574 onset CRC have the most highly increased expression of AlkBH8 as compared to other age
575 groups (Figure 6C). As AlkBH8 possesses two druggable domains[60,65] and could be a target for
576 future development of targeted therapies for early onset-CRC, we sought to experimentally
577 investigate the role of AlkBH8 in regulating the selenoproteome in CRC.

578 Two shRNA guides for AlkBH8 i-KD (sh3/4) were found to induce knockdown of AlkBH8 by 60%
579 (sh3) and 80% (sh4) respectively and were cloned into pLKO.1-Tet On for lentivirus based
580 production of stable doxycycline inducible KD cell lines (Figure 6D, S6D). In agreement with
581 prior literature, we observed that AlkBH8 i-KD led to an inability to translate GPx4 as western
582 blots in DLD1 stable shRNA cell lines revealed a sharp drop-off in GPx4 protein concentrations
583 at 72 hrs following doxycycline treatment (250ng/mL) in sh3/4 cell lines but not the NT control
584 line (Figure 6E). Furthermore, we observed a 40% reduction in TxnRD activity 72 hrs post
585 AlkBH8 KD (Figure 6F), supporting the ability of AlkBH8 i-KD to genetically replicate the broad
586 selenoprotein inhibitory mechanism of (S)-RSL3 and auranofin. To further investigate the
587 therapeutic potential of AlkBH8 in CRC the i-KD cell lines were maintained in doxycycline media
588 to assess growth and colony formation. A significant decrease in growth and colony formation
589 was observed across all tested CRC cell lines, with rescue observed by 10mM NAC co-
590 treatment (Figure 6G, S6E-F), supporting our hypothesis that AlkBH8 is a novel therapeutic
591 target in CRC through its ability to induce oxidative stress via modulation of the
592 selenoproteome.
593
594 **AlkBH8 is required for CRC xenograft growth and survival *in-vivo***
595 To further evaluate the effects of AlkBH8 i-KD in an *in-vivo* setting, we chose two of our top
596 responding cell lines (DLD1/SW480) for xenograft implantation. Both shAlkBH8 i-KD cell lines
597 (sh3/sh4) and shNT control cells were implanted (1 x 10^6/mouse) into the flank of NOD-SCID
598 mice. All mice were fed doxycycline chow (400 mg/kg) beginning on d1, and a subgroup of the
599 mice was additionally co-administered drinking water containing NAC (20mM). No alternative
600 food or water sources were provided while doxycycline chow and NAC water were continually
601 available *ad-libitum* throughout the study. In the DLD1 and SW480 cell lines, the shAlkBH8-3
602 and shAlkBH8-4 xenografts displayed a decrease in growth and a >50% reduction in final tumor
603 mass as compared to the shNT control. All xenografts displayed a complete rescue when mice

604 were co-administered NAC (Figure 7 A-D). TUNEL (terminal deoxynucleotidyl transferase dUTP
605 nick end labeling) staining was performed to assess endpoint cell death in xenograft tissue,
606 where we observed significantly increased cell death in the shAlkBH8 xenografts as compared
607 to the shNT control. NAC co-treatment fully rescued the increase in cell death, demonstrating
608 that in both cell lines AlkBH8 KD induced oxidative cell death in an *in-vivo* setting (Figure 7E).
609 Next, BrdU (bromodeoxyuridine) staining was performed to assess endpoint cellular proliferation
610 in xenograft tissue. The BrdU positive cell fraction significantly decreased in the shAlkBH8
611 xenografts as compared to the shNT control, with a full rescue observed upon NAC co-
612 treatment (Figure 7F). These data demonstrate that not only does AlkBH8 KD induce oxidative
613 cell death *in-vivo*, it is also capable of reducing the fraction of proliferating cells across multiple
614 shRNA constructs and two distinct CRC cell lines.
615
616 **Discussion**
617 Ferroptosis represents a targetable mechanism with high potential for cancer therapeutics. Yet,
618 ferroptosis research has predominantly relied on investigations using small molecules, which
619 can be confounded by unknown off-target effects. In this study we observe that despite broad
620 sensitivity to the GPx4 inhibitor (S)-RSL3, not all CRC cell lines are sensitive to genetic
621 depletion of GPx4, suggesting that at least some of the potency of (S)-RSL3 may stem from
622 GPx4-independent activity. Consequently, our findings shed light on the reduced potency
623 observed with the synthesis of next-generation GPx4 inhibitors such as JKE1674, where
624 heightened target engagement may paradoxically diminish activity. While RSL3 remains a
625 potent ferroptosis inducer, our data adds to its characterization and further cements that it is not
626 solely a GPx4 inhibitor.
627
628 While a large fraction of ferroptosis research still focuses on the central role of GPx4 as a lipid
629 peroxide detoxifying enzyme, our study suggests that the broader selenoproteome might

630 equally contribute to redox regulation. In addition to glutathione peroxidases, cells possess a
631 secondary method of peroxide detoxification, the peroxiredoxins (PRDXs) which rely on the
632 selenoprotein TxnRD1 for redox mediated turnover. Our data validate (S)-RSL3 as an inhibitor
633 of TxnRD1 and have led to observations that the DLD1 cell line has ~2-3-fold higher TxnRD
634 activity than other tested CRC cell lines. Overall, these data lead to a hypothesis that the DLD1
635 cell line may more heavily utilize the thioredoxin peroxidase system for regulation of intracellular
636 peroxides, perhaps explaining the observed insensitivity of these cells to JKE1674 and GPx4 i-
637 KD.
638
639 Recharacterization of the mechanism of (S)-RSL3 from a targeted inhibitor of GPx4 to a broad
640 inhibitor of the selenoproteome has revealed that (S)-RSL3 dually inhibits a binary system of
641 redox regulation in CRC cells, wherein the Txn and GPx systems are both essential to prevent
642 the toxic byproducts of ROS addiction. In line with this hypothesis, we observe that gold therapy
643 using the small molecule auranofin induces oxidative stress in CRC which can lead to
644 ferroptosis, with the exact mechanism of cell death occurring in a highly cell line and dose
645 dependent manner. In our studies, auranofin treatment in established tumors leads to reduced
646 tumor growth with observations of intra-tumoral necrosis suggesting that gold-based inhibition of
647 the selenoproteome can induce tumor cell death *in-vivo*. Furthermore, our studies of low dose
648 auranofin in AOM/DSS models of CRC demonstrate proof of concept that selenoprotein
649 inhibition can limit CRC progression, however due to the on-target toxicities of gold therapy this
650 approach has not yet been tested in the clinic.
651
652 These studies have revealed a novel therapeutic target in CRC: the tRNA methyltransferase
653 AlkBH8. Our data demonstrate the essential role of AlkBH8 for the growth of multiple CRC cell
654 lines. Supporting this data, whole-body knockout mice lacking AlkBH8 exhibit no discernible
655 defects, and individuals with homozygous AlkBH8 mutations show a non-lethal phenotype,

656 indicating tolerability to complete loss of AlkBH8 activity[57,66,67]. Importantly, AlkBH8 features two
657 druggable domains, an AlkB Fe(II)/α-ketoglutarate-dependent dioxygenase domain and a
658 methyltransferase domain. Although full-length recombinant AlkBH8 and its substrates remain
659 poorly characterized, we anticipate that their development will facilitate small molecule inhibitor
660 discovery, potentially yielding novel targeted therapies for CRC.
661
662 In conclusion, our exploration into the selenoproteome highlights the therapeutic potential of this
663 underexplored protein class. Selenium, and by extension selenocysteine, is orders of magnitude
664 more efficient in reacting with and detoxifying ROS as compared to the sulfur containing
665 cysteine[68], coinciding with the majority of selenoproteins functioning as antioxidant enzymes in
666 the regulation of oxidative stress. However, only a fraction of the selenoproteome has been
667 investigated to decipher their roles in human biology, and even less for their involvement in
668 cancer development and progression. While our approaches employing AlkBH8 KD, gold
669 therapy, and chloroacetamide warheads to target the selenoproteome yield non-selective
670 inhibition of the selenoproteome, we posit that deeper investigations into the biology of
671 selenoproteins may not only advance our understanding of cellular redox regulation, but also
672 unveil novel therapeutic targets for the treatment of human disease.
673
674 **Acknowledgements**
675 The authors would like to acknowledge the members of the Shah and Koutmos laboratories for
676 project feedback and manuscript editing. This work was funded by NIH grants R01CA148828,
677 R01CA245546, and R01DK095201 (Y.M.S.), UMCCC Core grant P30CA046592 (Y.M.S.),
678 CA286898 and GM117141 (M.K.), NIH/NIGMS grant R01GM132129 (J.A.P.), NIH grant
679 R01DK124384 to JDM, and R01CA262439 (Z.T.S.). Sumeet Solanki was supported by a
680 Crohn's and Colitis Foundation Research fellow award (623914) and the American Heart
681 Association postdoctoral fellowship (19POST34380588). JDM holds patents for methods for

682 modulating ferritinophagy. JDM reports research support from Novartis and Casma
683 Therapeutics and has consulted for Third Rock Ventures and Skyhawk Therapeutics, all
684 unrelated to the work
685
686 **Author Contributions**
687 SLD, MK, and YMS initiated the project, performed or directed all experiments, and wrote the
688 manuscript. SD assisted with the majority of experiments as an undergraduate assistant. SS
689 was heavily involved in training and assistance for in-vivo studies. LZ, MOD, NKD, CC, HNB,
690 YZ, NJR, EM, JH, ZS, and IT assisted with in-vitro, bioinformatic, and/or in-vivo experiments.
691 YQ and BWLN assisted with CETSA experiments. MS, JP, and JM performed Mass
692 Spectrometry studies. AB and NN synthesized RSL3 derivatives. MK and YMS provided funding
693 and mentorship for SLD throughout the project.

Figure 1

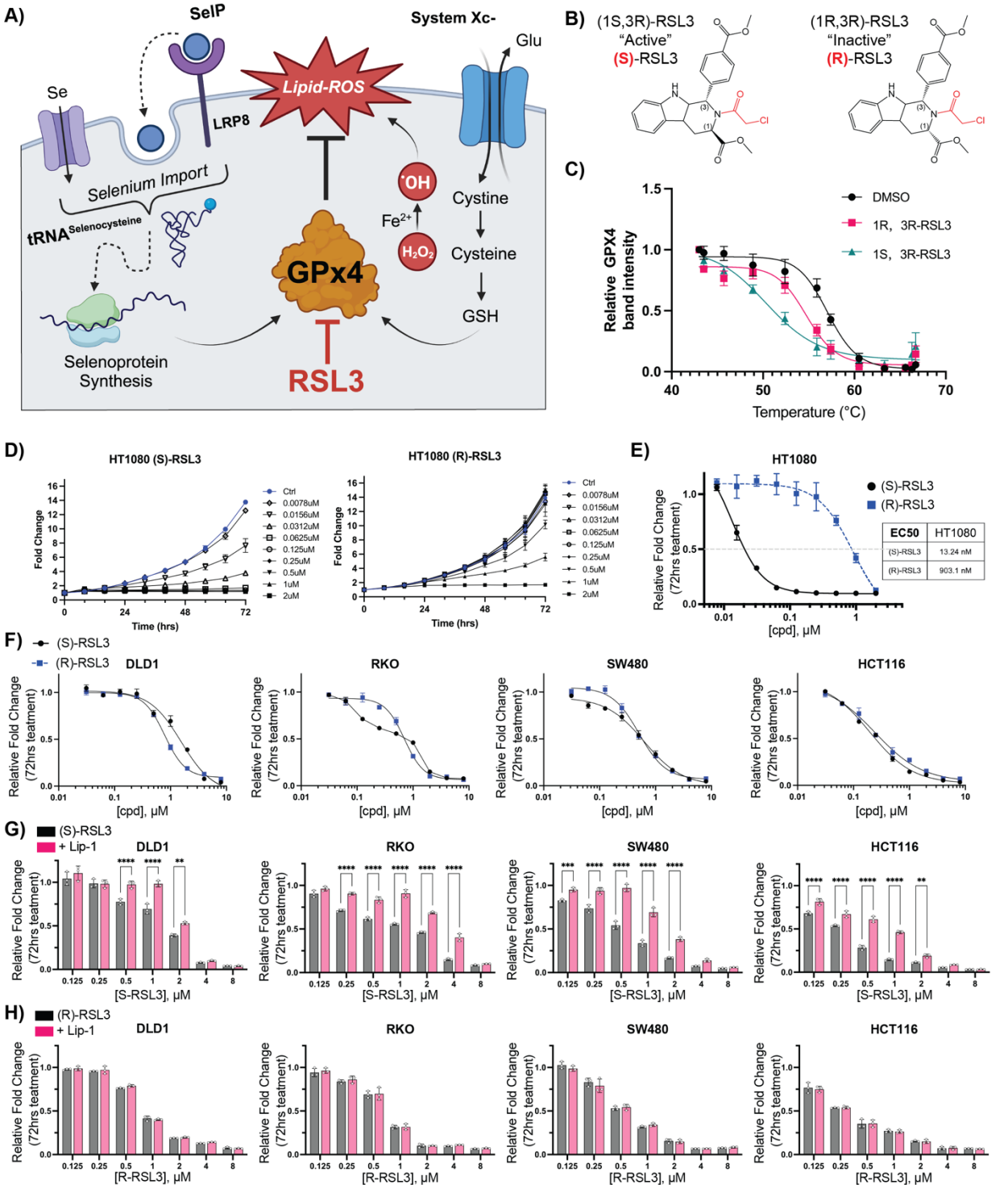
A)
SelP
System Xc-
Glu
Se
LRP8
Lipid-ROS
Selenium Import
tRNA Selenocysteine
•OH
Fe2+
H2O2
Cystine
Cysteine
GSH
GPx4
Selenoprotein Synthesis
RSL3
B)
(1S,3R)-RSL3 "Active" (S)-RSL3
(1R,3R)-RSL3 "Inactive" (R)-RSL3
C)
DMSO
1R, 3R-RSL3
1S, 3R-RSL3
Relative GPX4 band intensity
Temperature (°C)
D)
HT1080 (S)-RSL3
HT1080 (R)-RSL3
Fold Change
Time (hrs)
Ctrl
0.0078uM
0.0156uM
0.0312uM
0.0625uM
0.125uM
0.25uM
0.5uM
1uM
2uM
E)
HT1080
(S)-RSL3
(R)-RSL3
Relative Fold Change (72hrs teatment)
[cpd], μM
EC50 HT1080
(S)-RSL3 13.24 nM
(R)-RSL3 903.1 nM
F)
(S)-RSL3
(R)-RSL3
DLD1
RKO
SW480
HCT116
Relative Fold Change (72hrs teatment)
[cpd], μM
G)
(S)-RSL3
+ Lip-1
[S-RSL3], μM
H)
(R)-RSL3
+ Lip-1
[R-RSL3], μM

Figure 1: Defining the ferroptotic window of S-RSL3 in CRC cell lines.
A) Schematic of ferroptosis demonstrating the role of of GPx4 to detoxify ROS induced lipid peroxides (Lipid-ROS) is regulated by GSH synthesis driven by System Xc- import of cystine and selenium availability in part by LRP8 which is then incorporated into the GPx4 polypeptide by tRNA-selenocysteine. **B)** Structures of (1S,3R)-RSL3 and (1R,3R)-RSL3. **C and D)** Cell growth assay normalized to untreated control at 72 hr following (S) or (R) RSL3 treatment in HT1080 and CRC cell lines. **E)** Results of cell growth assay from C-D where 72 hr growth of cells treated with indicated doses of (S) and (R) RSL3 is normalized to 72 hr growth of vehicle treated control wells to calculate EC50 value ("Results of 72 hr cell growth assay"). **F)** Results of 72 hr cell growth assay of (S) and (R) RSL3 across a panel of CRC cell lines. **G-H)** Statistical analysis of results of 72 hr cell growth assay of (S) and (R) RSL3 co-treated with liproxstatin-1 (Lip-1) (1 μM) *: $p < 0.05$, **: $p < 0.01$, ***: $p < 0.001$, ****: $p < 0.0001$

Figure S1

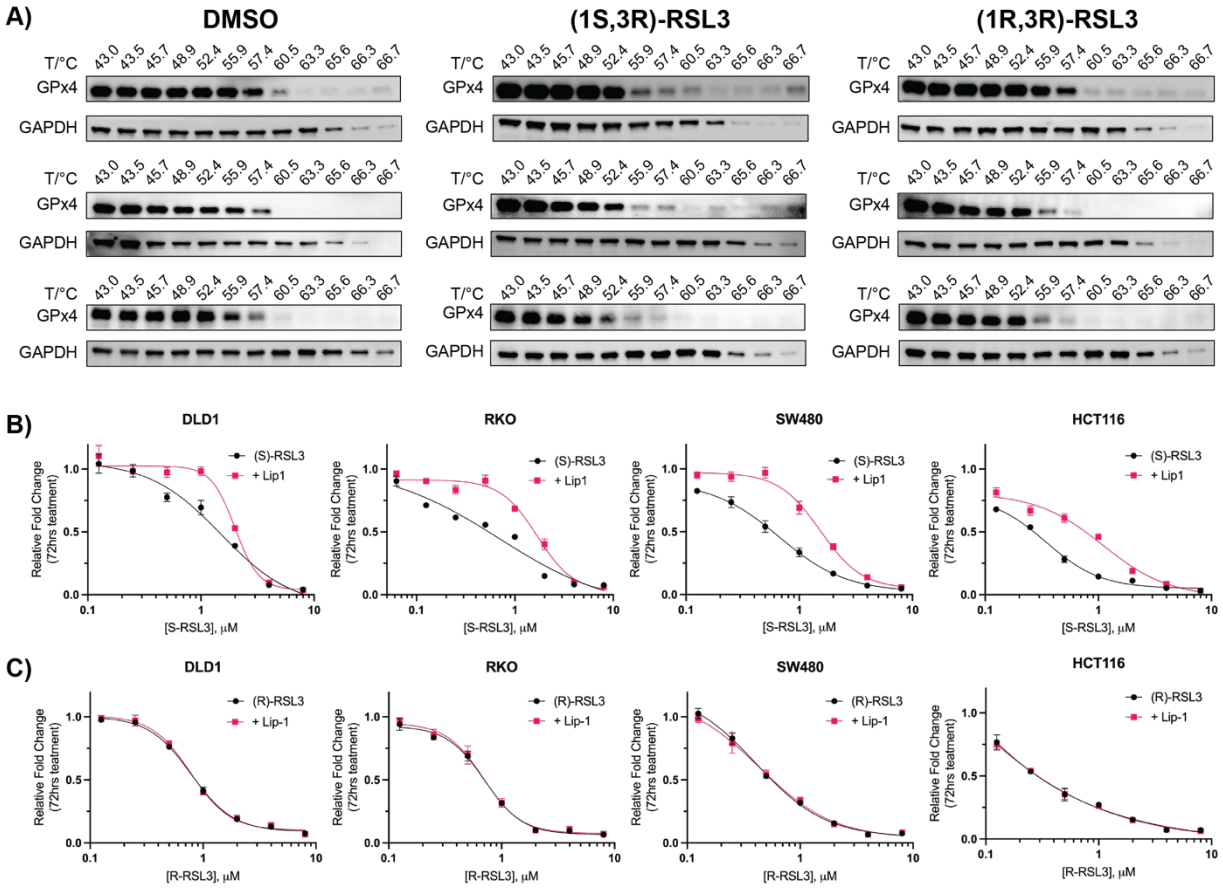

Figure S1
A) Western blots of GPx4 CETSA experiments used for generation of Figure 1C. 293T cells were treated with compound as indicated (10μM, 1hr) and lysates were heated to the indicated temperature before pelleting precipitated proteins **B and C)** Cell growth normalized to untreated control at 72 hr following (S) or (R) RSL3 dose response +/- Liproxstatin-1 (1μM) co-treatment in CRC cell lines.

Figure 2

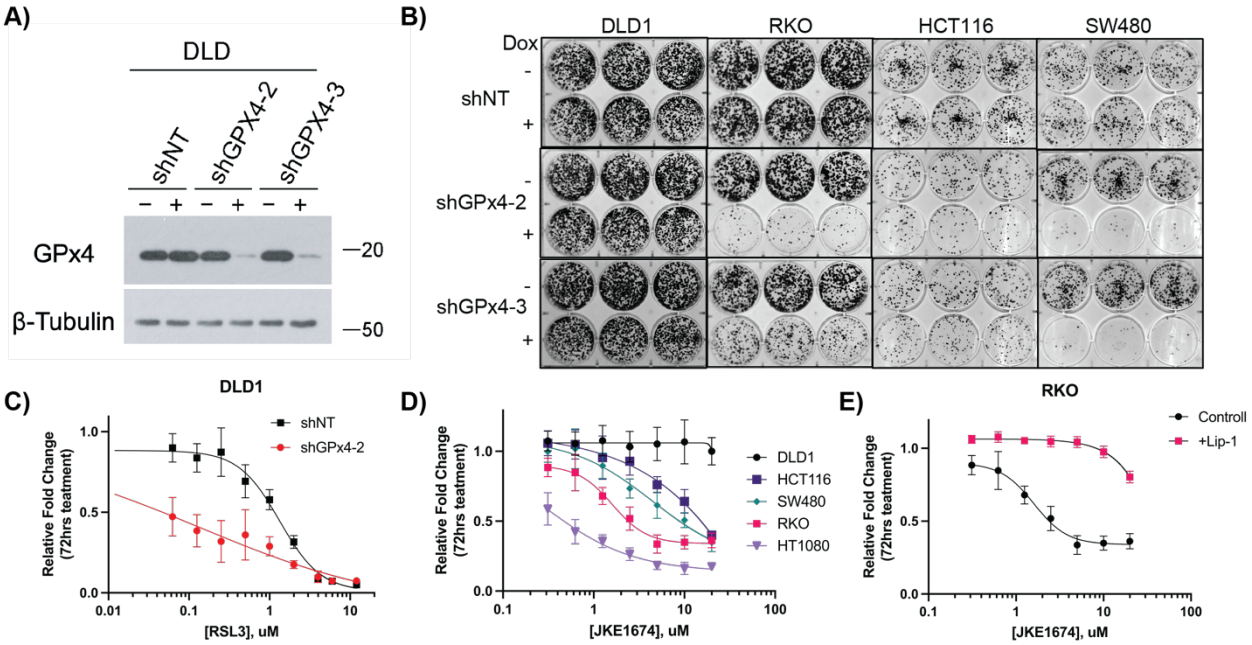

Figure 2: Elucidating the role of GPx4 in CRC cell lines.
A) Western blot of stable DLD1 doxycycline inducible shRNA cell lines (shNT, shGPx4-2, shGPx4-3), +/- doxycycline treatment (250 ng/mL) assessed at 72 hrs. β-Tubulin was used as a loading control. **B)** Colony formation assays of indicated stable shGPx4 or shNT cell lines treated +/- doxycycline (250ng/mL) assessed at 2 weeks. **C)** Results of 72 hr cell growth assay following (S)-RSL3 treatment in DLD1 shNT vs shGPx4-2 cell lines, pre-treated with doxycycline (250 ng/mL) for 72 hrs prior to addition of (S)-RSL3. **D)** Results of 72 hr cell growth assay following JKE1674 dose response of CRC cell lines and HT1080 cells. **E)** Results of 72 hr cell growth assay following JKE1674 dose response of the RKO CRC cell line +/- Lip-1 (1 μM) co-treatment

Figure S2

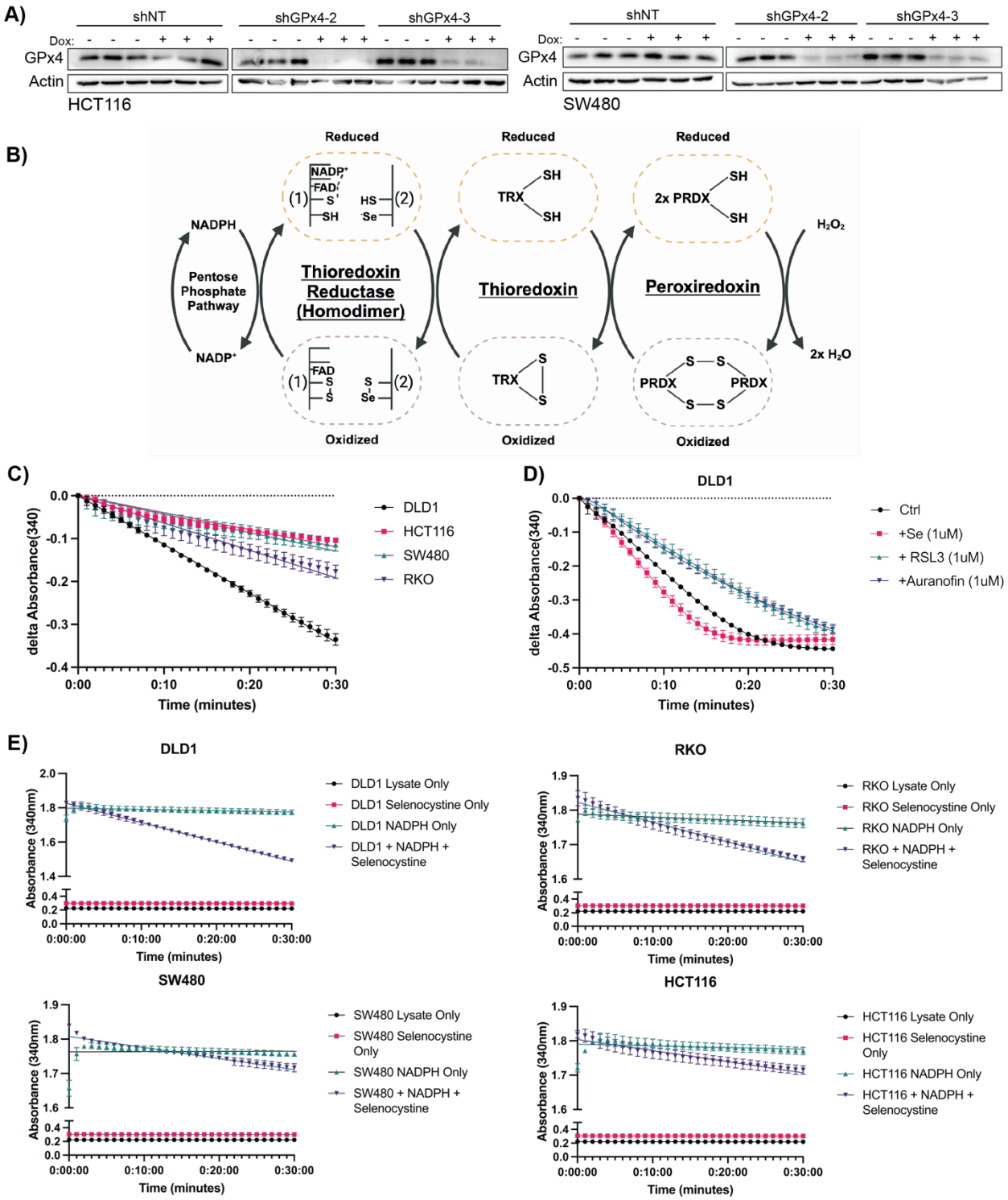

Figure S2

A) Western Blots of GPx4 levels in HCT116 and SW480 shNT, shGPx4-2, shGPx4-3 cell lines following 72hr treatment with doxycycline (250 ng/mL) **B)** Schematic of the mechanism of the Thioredoxin Reductase-Peroxiredoxin system, where NADPH from the Pentose Phosphate Pathway is utilized in the selenoprotein Thioredoxin Reductase to recycle oxidized 2-Cys Peroxiredoxins after the redox mediated detoxification of hydrogen peroxide, forming a Peroxiredoxin dimer. The peroxiredoxin dimer is reduced through oxidation of thioredoxin, and oxidized thioredoxin is reduced by TxnRD1 **C)** Thioredoxin Reductase Kinetic Activity Assay measuring NADPH consumption through reduction of NADPH absorbance at 340 nm upon addition of NADPH and Selenocystine to cell lysates of indicated CRC cell lines **D)** Modulation of the thioredoxin reductase activity assay after 24hr treatment of DLD1 cells as indicated. **E)** Internal controls utilized for the thioredoxin reductase kinetic activity assay. Absorbance at 340 nm was measured every 60 s for 30 min on a Cytation 5 plate reader. Wells contained either lysate only, lysate + selenocystine, lysate + NADPH, or lysate + selenocystine & NADPH as indicated. 3 technical replicates were averaged for each point and plotted as mean +/- SD

Figure 3

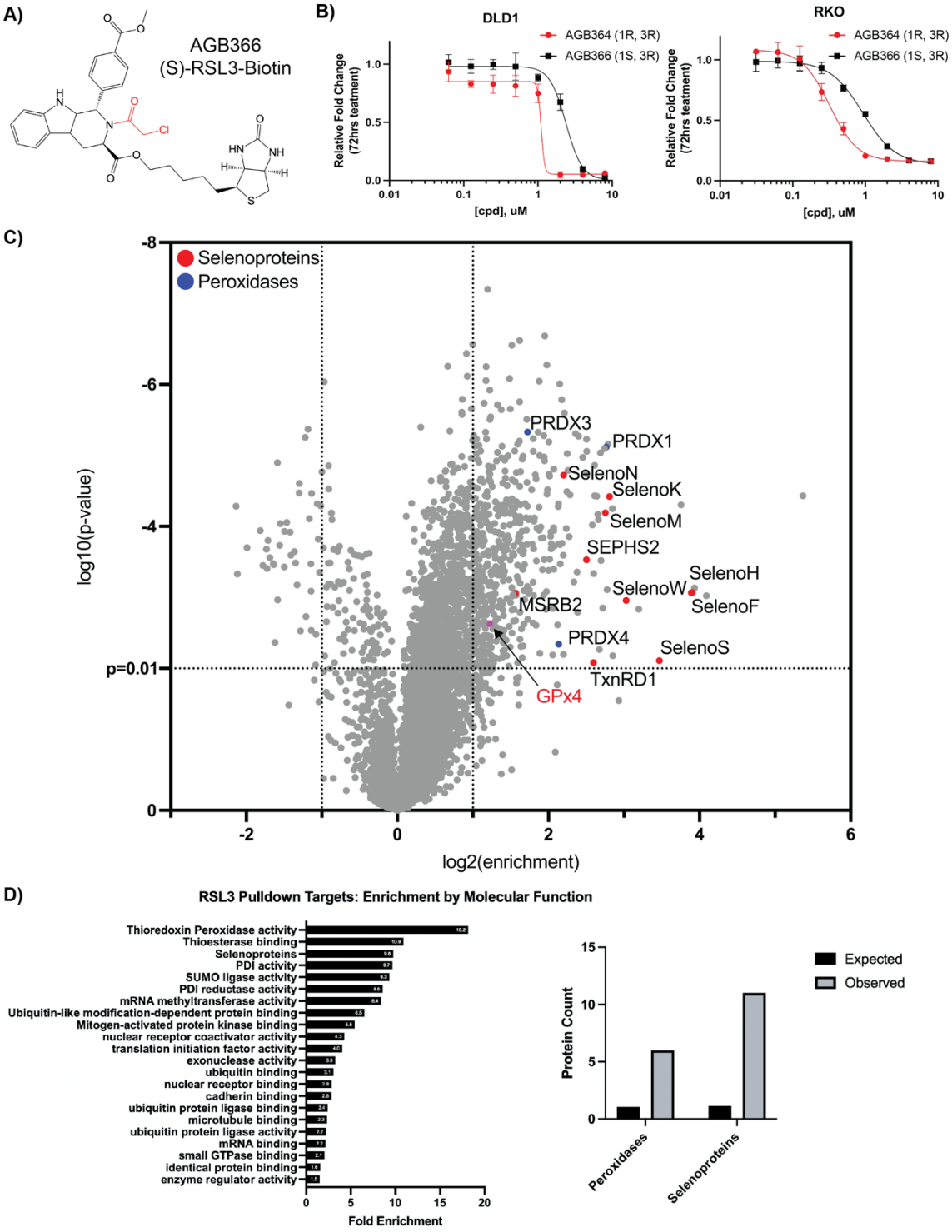

Figure 3: Affinity pulldown-mass spectrometry redefines RSL3 as a selenoprotein inhibitor.

A) AGB366, a biotinylated RSL3 derivative. **B)** Results of 72 hr cell growth assay following AGB364/366 dose response treatment in DLD1 and RKO cells. **C)** Affinity-pulldown mass spectrometry analysis of AGB366 ((S)-RSL3-Biotin) from RKO lysate with targets of interest identified. **D)** RSL3 Pulldown targets protein class enrichment (PANTHER) and number of peroxidases and selenoproteins observed in the AGB366 pulldown dataset vs. expected by random chance.

Figure S3

A)

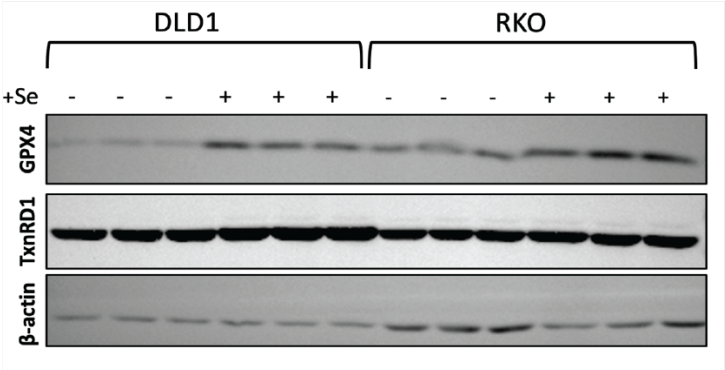

B)

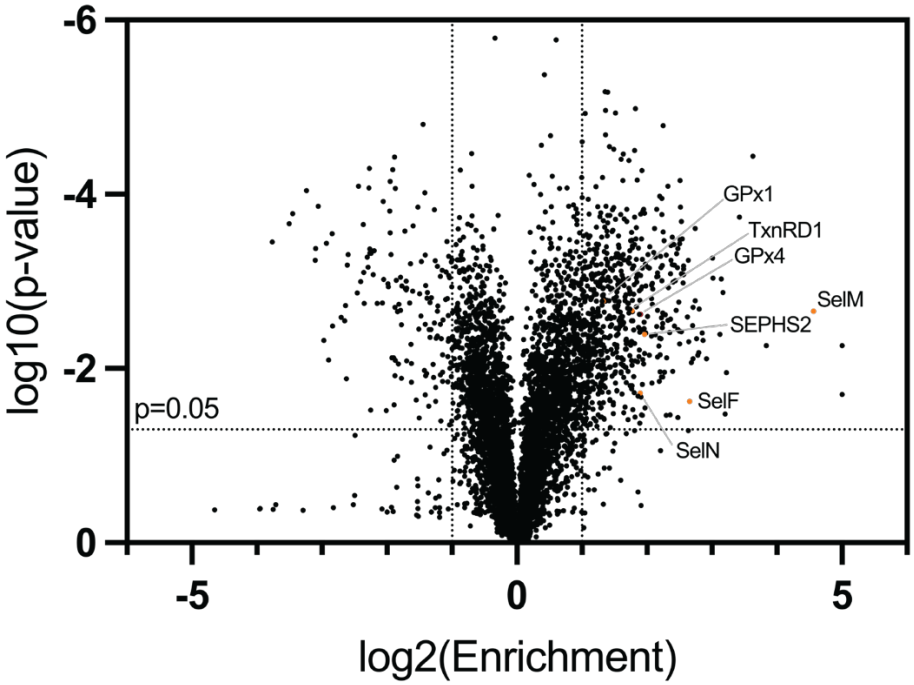

Figure S3
A) Western blot analysis of GPx4 and TxnRD1 protein levels in DLD1 and RKO cell lines following 24 hr supplemention with 1 μM Sodium Selenite. **B)** AP-MS results of Biotin-Cpd24 pulldown compared to Cpd24 mock pulldown control. Significant selenoproteins hits are identified

Figure 4

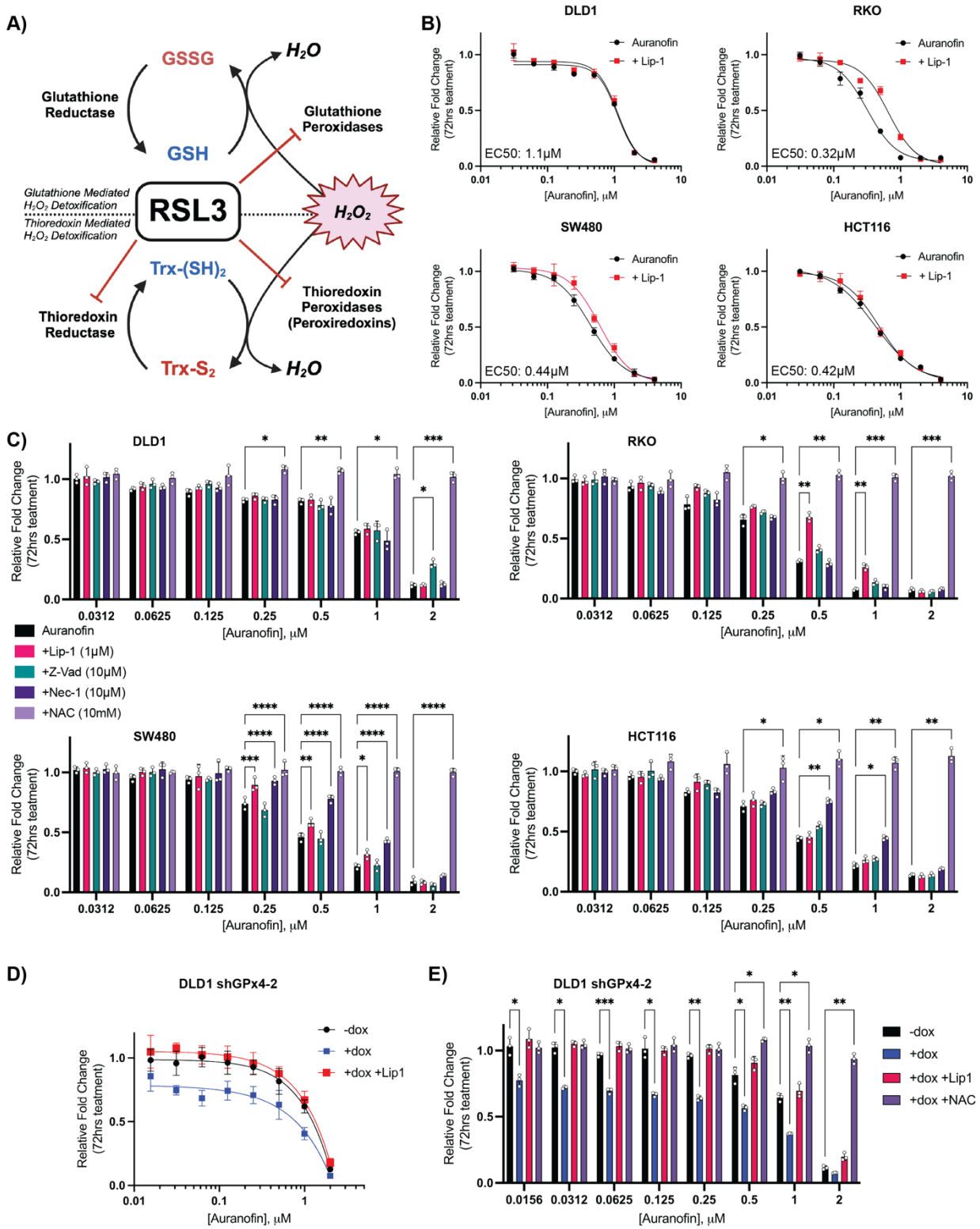
A)
GSSG
H_2O
Glutathione Reductase
Glutathione Peroxidases
GSH
Glutathione Mediated H_2O_2 Detoxification
RSL3
H_2O_2
Thioredoxin Mediated H_2O_2 Detoxification
Trx-(SH)$_2$
Thioredoxin Peroxidases (Peroxiredoxins)
Thioredoxin Reductase
Trx-S$_2$
H_2O
B)
DLD1
RKO
SW480
HCT116
Auranofin
+ Lip-1
EC50: 1.1μM
EC50: 0.32μM
EC50: 0.44μM
EC50: 0.42μM
Relative Fold Change (72hrs teatment)
[Auranofin], μM
C)
Auranofin
+Lip-1 (1μM)
+Z-Vad (10μM)
+Nec-1 (10μM)
+NAC (10mM)
D)
DLD1 shGPx4-2
-dox
+dox
+dox +Lip1
E)
+dox +NAC

Figure 4: Auranofin induces ferroptosis in CRC.
A) Schematic of the new proposed mechanism of RSL3 activity where RSL3 as a pan-inhibitor of the selenoproteome can inhibit both glutathione and thioredoxin reductases as well as peroxiredoxins. **B)** Results of 72 hr cell growth assay following auranofin +/- Lip-1 (1 μM) co-treatment across a panel of CRC cells. **C)** Statistical analysis of 72 hr cell growth assay rescue by indicated co-treatments: Lip-1 (1 μM), Z-vad-FMK (10 μM), NAC (10 mM), Nec1 (10 μM). Cells were pre-treated with rescue agent for 24 hr prior to addition of auranofin **D)** Results of 72 hr cell growth assay of the DLD1 shGPx4-2 cell line treated as indicated (vehicle treated control, 250 ng/mL doxycycline, 1 μM Lip-1). Cells were pretreated with doxycycline or vehicle (ddH_2O) for 72 hr prior to first imaging and treatment with auranofin +/- Lip-1 **E)** Statistical analysis of 72 hr cell growth assay of DLD1 shGPx4-2 cells measuring deviation of growth response following auranofin treatment from control (-dox) by doxycycline treatment (+dox) +/- co-treatment with Lip-1 (1 μM) or NAC (10mM)
*: $p < 0.05$, **: $p < 0.01$, ***: $p < 0.001$, ****: $p < 0.0001$

Figure S4

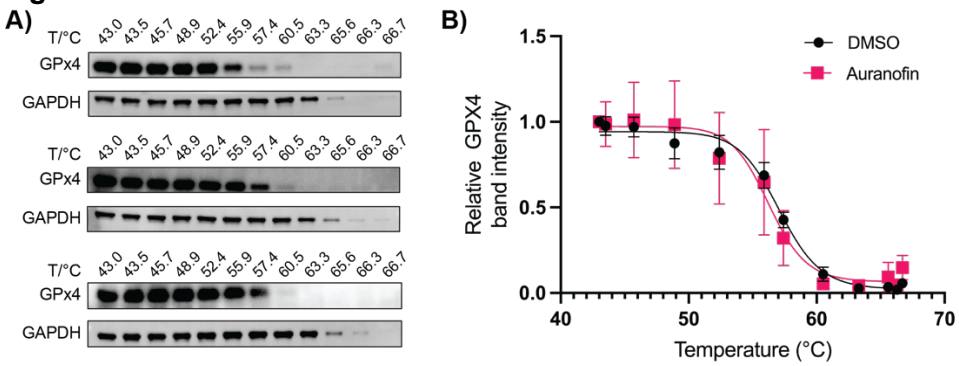

Figure S4
A) CETSA analysis of GPx4 protein thermal stability following auranofin treatment (10 μM**,** 1 hr) in 293T cells. DMSO controls are included as Figure S1A. **B)** Results of CETSA analysis from A calculating deviation of GPx4 band intensity between DMSO treated and auranofin treated cells (DMSO controls shown as Fig S1A)

Figure 5

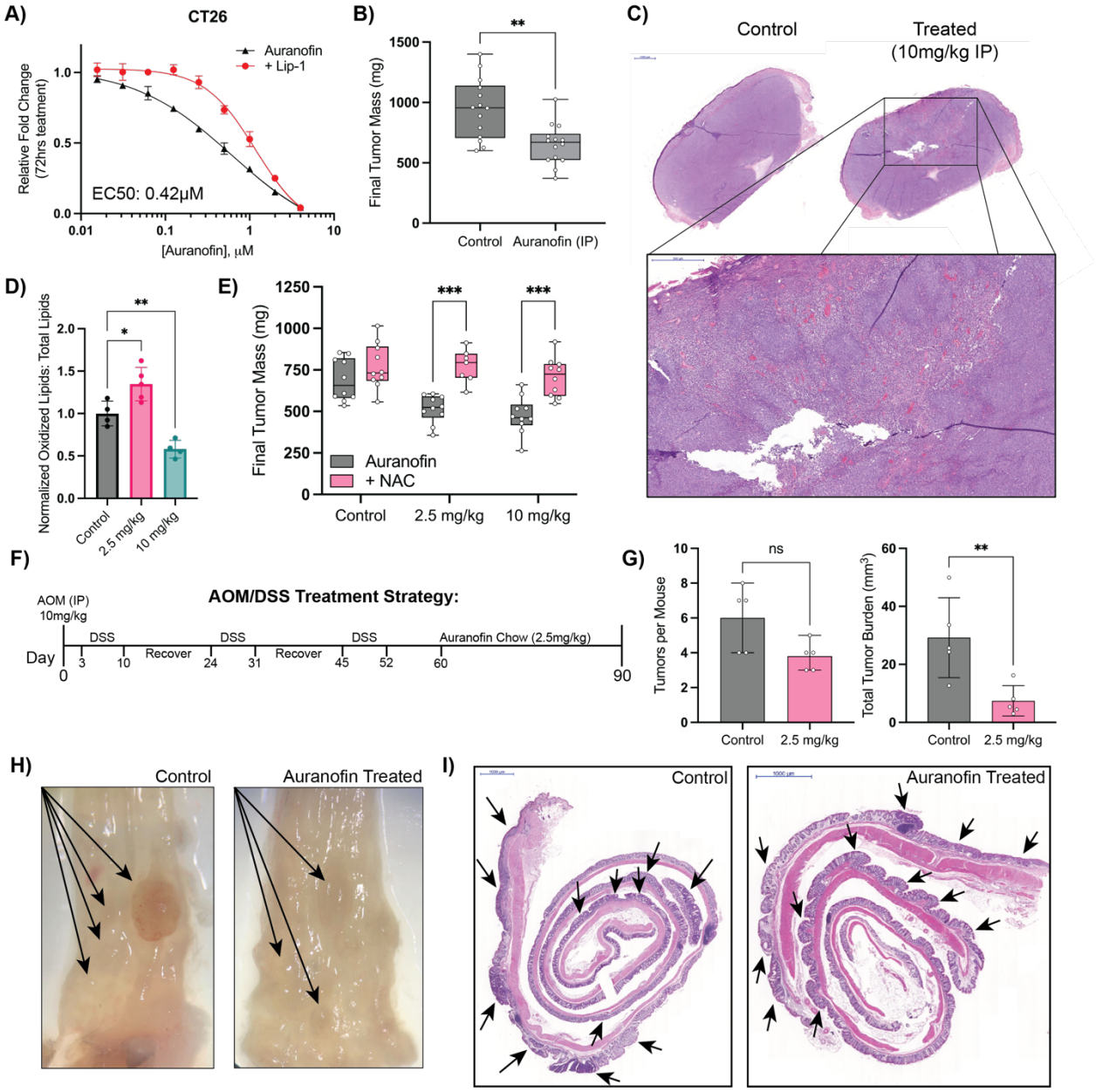

Figure 5: Auranofin is an effective treatment in *in-vivo* models of CRC.
A) Results of 72 hr cell growth assay of auranofin dose response +/- Lip-1 (1 μM) co-treatment in CT26 cells. **B)** Final tumor mass of CT26 xenograft studies in Balb/c mice treated with vehicle or auranofin IP injection (10mg/kg daily) **C)** H&E staining of Auranofin treated vs control tumor with higher magnification of a region of interest in the treated tumor. **D)** Flow cytometry measurements of Lipid-ROS levels in control vs auranofin treated CT26 xenografts. **E)** Final tumor mass of CT26 xenografts treated with indicated doses of auranofin chow +/- NAC (20mM) drinking water. **F)** Schematic of AOM/DSS model of colitis induced colorectal cancer and subsequent auranofin treatment **G)** Quantification of tumor number and total tumor burden (mm^3) per mouse colon following AOM/DSS induction and subsequent auranofin treatment. **H)**

Representative microscopy pictures of control and treated colons (Auranofin 2.5 mg/kg) with visually detectable tumors marked by arrows. **I)** H&E staining of swiss-rolled colons from C. Notable regions of dysplasia are marked by arrows.
*: $p < 0.05$, **: $p < 0.01$, ***: $p < 0.001$, ****: $p < 0.0001$

Figure S5

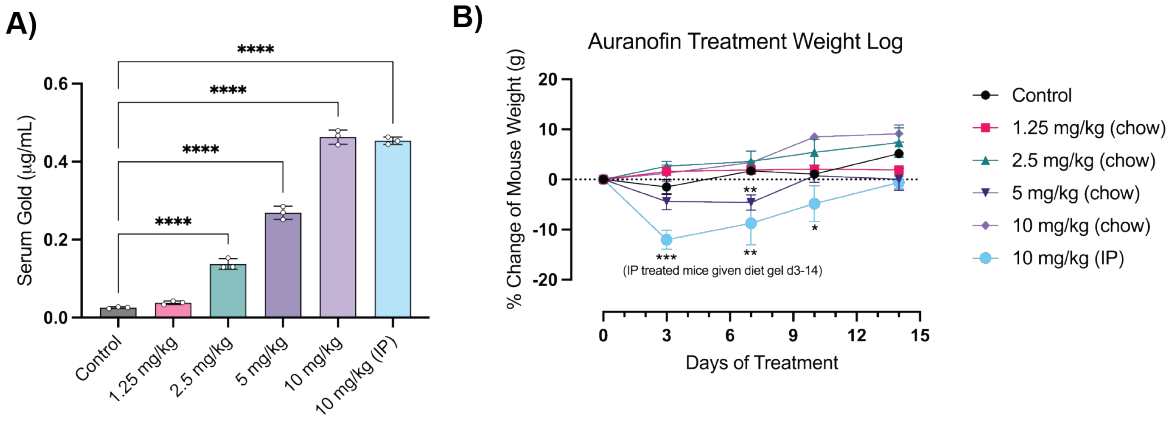

Figure S5
A) Terminal serum gold measurements by ICPMS of non tumor bearing control mice (C57Bl/6J) treated with indicated dosing of auranofin via chow or IP as indicated for two weeks. **B)** Weight log of non tumor bearing control mice treated with auranofin via chow or IP as indicated. IP treated mice were administered supplemental diet gel beginning d3 following rapid initial weight loss

Figure 6

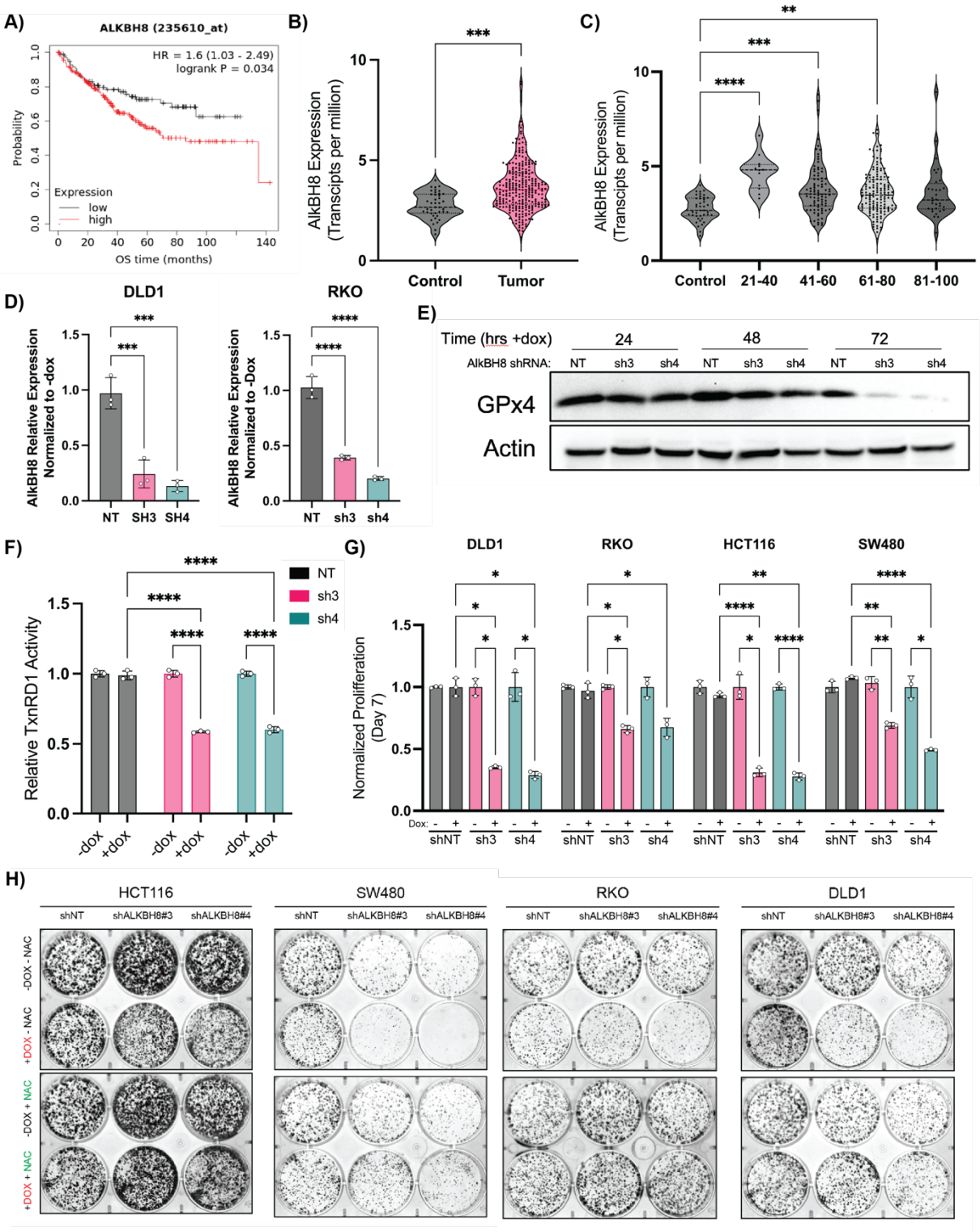

Figure 6: AlkBH8 is a potential therapeutic target in CRC.

A) Kaplan-Meier overall survival analysis of CRC patients based on AlkBH8 expression as measured by RNA-Seq. **B)** RNA analysis of colorectal adenocarcinoma (COAD) tumor samples

vs normal tissue (TCGA) analyzed for AlkBH8 expression. **C)** RNA analysis of colorectal adenocarcinoma (COAD) tumor samples vs normal tissue (TCGA) analyzed for AlkBH8 expression and separated by age group. **D)** qPCR measurement of AlkBH8 mRNA levels in NT and shRNA cell lines following 72 hrs treatment with doxycycline (250ng/mL). Normalized to untreated control. **E)** Western blot analysis of GPx4 protein levels in DLD1 shNT, shAlkBH8-3, and shAlkBH8-4 cell lines following doxycycline treatment (250ng/mL) for indicated times. **F)** TxnRD1 activity in DLD1 shNT, shAlkBH8-3, and shAlkBH8-4 cell lines following doxycycline treatment (250ng/mL) for 72hrs **G)** Cell growth assay at 7 days of indicated CRC cell lines stably transduced with either shNT, shAlkBH8-3, or shAlkBH8-4 and continually treated with doxycycline (250ng/mL). Normalized to untreated control growth at d7. **H)** CFA analysis of CRC cell lines stably transduced with either shNT, shAlkBH8-3, or shAlkBH8-4 as indicated and continually treated +/- doxycycline (250ng/mL) and +/- NAC (10mM) as indicated
*: $p < 0.05$, **: $p < 0.01$, ***: $p < 0.001$, ****: $p < 0.0001$

Figure S6

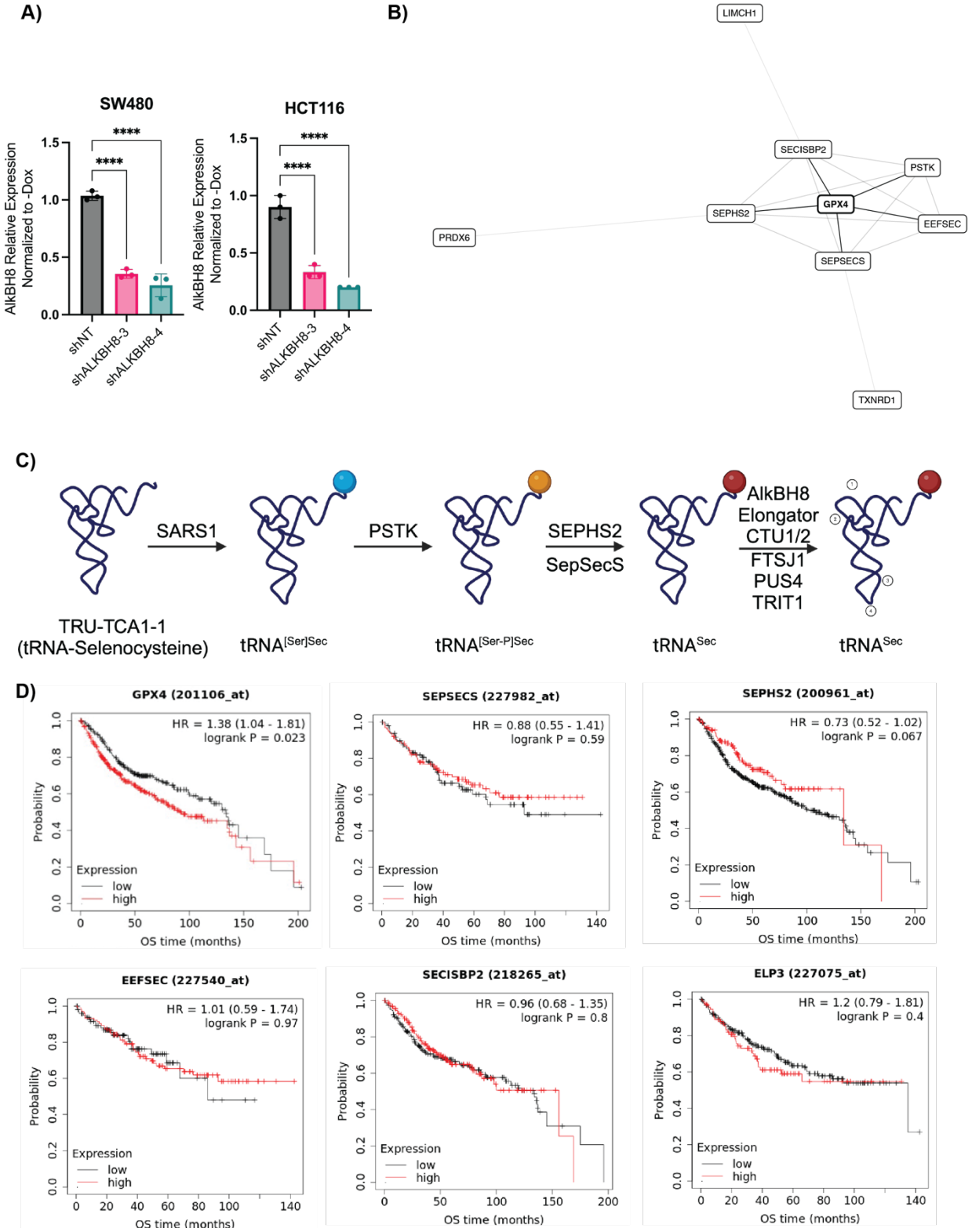
A)
SW480
HCT116
AlkBH8 Relative Expression Normalized to -Dox
****
shNT
shALKBH8-3
shALKBH8-4
B)
LIMCH1
SECISBP2
PSTK
SEPHS2
GPX4
EEFSEC
PRDX6
SEPSECS
TXNRD1
C)
SARS1
PSTK
SEPHS2
SepSecS
AlkBH8
Elongator
CTU1/2
FTSJ1
PUS4
TRIT1
TRU-TCA1-1
(tRNA-Selenocysteine)
tRNA[Ser]Sec
tRNA[Ser-P]Sec
tRNASec
tRNASec
D)
GPX4 (201106_at)
HR = 1.38 (1.04 - 1.81)
logrank P = 0.023
SEPSECS (227982_at)
HR = 0.88 (0.55 - 1.41)
logrank P = 0.59
SEPHS2 (200961_at)
HR = 0.73 (0.52 - 1.02)
logrank P = 0.067
EEFSEC (227540_at)
HR = 1.01 (0.59 - 1.74)
logrank P = 0.97
SECISBP2 (218265_at)
HR = 0.96 (0.68 - 1.35)
logrank P = 0.8
ELP3 (227075_at)
HR = 1.2 (0.79 - 1.81)
logrank P = 0.4
Probability
Expression
low
high
OS time (months)

Figure S6
A) qPCR analysis of shNT or shAlkBH8 HCT116/SW480 cell lines measuring AlkBH8 mRNA expression following 72 hr dox treatment normalized to -dox control. **B)** CRISPR co-essentiality network map of GPx4 co-dependencies with distances indicating degree of co-essentiality. **C)** Biosynthetic pathway of tRNA-Selenocysteine where following transcription of the TRU-TCA1-1 gene, the tRNA-Sec mRNA undergoes on-tRNA biosynthesis of selenocysteine and post-transcriptional modification. **D)** Km plots of select genes in the tRNA-sec pathway with sufficient patient samples to perform a high-powered analysis

Figure 7

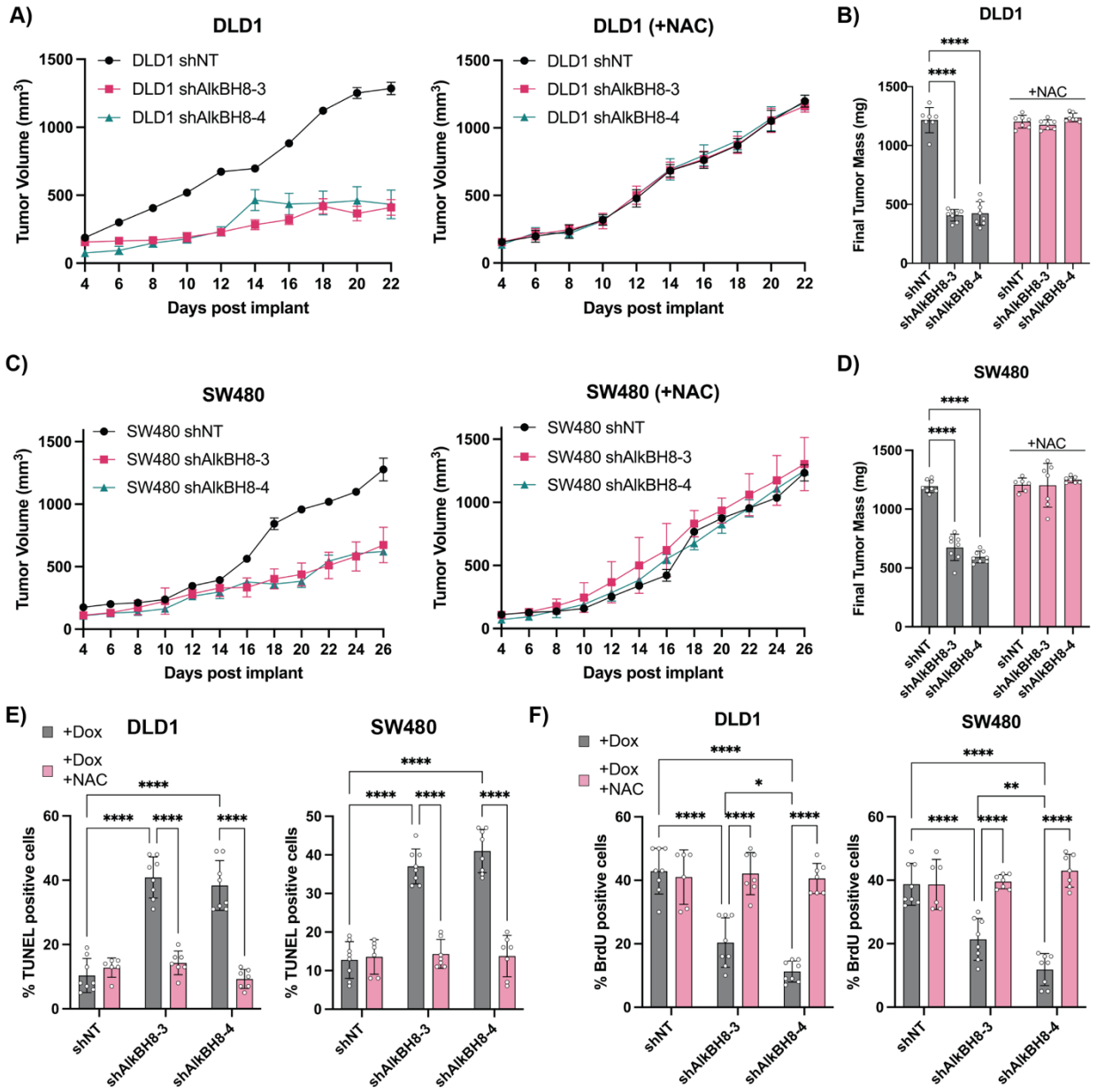

Figure 7: AlkBH8 i-KD induces oxidative stress dependent cell death *in-vivo*
A) Tumor volume measurements taken by caliper of DLD1 shNT, shAlkBH8-3, and shAlkBH8-4 xenografts in NOD/SCID mice treated with doxycycline chow +/- co-administration of NAC drinking water. **B)** Final tumor mass of DLD1 xenografts from A. **C)** Tumor volume measurements taken by caliper of SW480 shNT, shAlkBH8-3, and shAlkBH8-4 xenografts in NOD/SCID mice treated with doxycycline chow co-administration of NAC drinking water. **D)** inal tumor mass of SW480 xenografts from C. **E)** Analysis of TUNEL staining (% positive cells) of DLD1 and SW480 xenografts +/- NAC co-treatment. **F)** Analysis of BrdU staining (% positive cells) of DLD1 and SW480 xenografts

References

1. Siegel, R. L., Giaquinto, A. N. & Jemal, A. Cancer statistics, 2024. *CA. Cancer J. Clin.* **74**, 12–49 (2024).
2. Rawla, P., Sunkara, T. & Barsouk, A. Epidemiology of colorectal cancer: incidence, mortality, survival, and risk factors. *Przegląd Gastroenterol.* **14**, 89–103 (2019).
3. Siegel, R. L., Wagle, N. S., Cercek, A., Smith, R. A. & Jemal, A. Colorectal cancer statistics, 2023. *CA. Cancer J. Clin.* **73**, 233–254 (2023).
4. Tomasetti, C., Marchionni, L., Nowak, M. A., Parmigiani, G. & Vogelstein, B. Only three driver gene mutations are required for the development of lung and colorectal cancers. *Proc. Natl. Acad. Sci.* **112**, 118–123 (2015).
5. Raskov, H., Søby, J. H., Troelsen, J., Bojesen, R. D. & Gögenur, I. Driver Gene Mutations and Epigenetics in Colorectal Cancer. *Ann. Surg.* **271**, 75 (2020).
6. Cercek, A. *et al.* PD-1 Blockade in Mismatch Repair-Deficient, Locally Advanced Rectal Cancer. *N. Engl. J. Med.* **386**, 2363–2376 (2022).
7. Jin, Z. & Sinicrope, F. A. Prognostic and Predictive Values of Mismatch Repair Deficiency in Non-Metastatic Colorectal Cancer. *Cancers* **13**, 300 (2021).
8. Chen, B. *et al.* PTEN-induced kinase PINK1 supports colorectal cancer growth by regulating the labile iron pool. *J. Biol. Chem.* **299**, 104691 (2023).
9. Schwartz, A. J. *et al.* Hepcidin sequesters iron to sustain nucleotide metabolism and mitochondrial function in colorectal cancer epithelial cells. *Nat. Metab.* **3**, 969–982 (2021).
10. Singhal, R. *et al.* HIF-2α activation potentiates oxidative cell death in colorectal cancers by increasing cellular iron. *J. Clin. Invest.* **131**, 143691 (2021).

11. Liu, Z. *et al.* Iron promotes glycolysis to drive colon tumorigenesis. *Biochim. Biophys. Acta Mol. Basis Dis.* **1869**, 166846 (2023).

12. Dixon, S. J. *et al.* Ferroptosis: an iron-dependent form of nonapoptotic cell death. *Cell* **149**, 1060–1072 (2012).

13. Winterbourn, C. C. Toxicity of iron and hydrogen peroxide: the Fenton reaction. *Toxicol. Lett.* **82–83**, 969–974 (1995).

14. Jiang, X., Stockwell, B. R. & Conrad, M. Ferroptosis: mechanisms, biology and role in disease. *Nat. Rev. Mol. Cell Biol.* **22**, 266–282 (2021).

15. Chen, X., Comish, P. B., Tang, D. & Kang, R. Characteristics and Biomarkers of Ferroptosis. *Front. Cell Dev. Biol.* **9**, (2021).

16. Zilka, O. *et al.* On the Mechanism of Cytoprotection by Ferrostatin-1 and Liproxstatin-1 and the Role of Lipid Peroxidation in Ferroptotic Cell Death. *ACS Cent. Sci.* **3**, 232–243 (2017).

17. Yang, W. S. *et al.* Regulation of Ferroptotic Cancer Cell Death by GPX4. *Cell* **156**, 317–331 (2014).

18. Weaver, K. & Skouta, R. The Selenoprotein Glutathione Peroxidase 4: From Molecular Mechanisms to Novel Therapeutic Opportunities. *Biomedicines* **10**, 891 (2022).

19. Moghadaszadeh, B. & Beggs, A. H. Selenoproteins and Their Impact on Human Health Through Diverse Physiological Pathways. *Physiol. Bethesda Md* **21**, 307–315 (2006).

20. Labunskyy, V. M., Hatfield, D. L. & Gladyshev, V. N. Selenoproteins: molecular pathways and physiological roles. *Physiol. Rev.* **94**, 739–777 (2014).

21. Ingold, I. *et al.* Selenium Utilization by GPX4 Is Required to Prevent Hydroperoxide-Induced Ferroptosis. *Cell* **172**, 409-422.e21 (2018).

22. Sui, X. *et al.* RSL3 Drives Ferroptosis Through GPX4 Inactivation and ROS Production in Colorectal Cancer. *Front. Pharmacol.* **9**, 1371 (2018).

23. Solanki, S. *et al.* Dysregulated Amino Acid Sensing Drives Colorectal Cancer Growth and Metabolic Reprogramming Leading to Chemoresistance. *Gastroenterology* **164**, 376-391.e13 (2023).

24. Huang, W. *et al.* Dietary Iron Is Necessary to Support Proliferative Regeneration after Intestinal Injury. *J. Nutr.* **154**, 1153–1164 (2024).

25. Győrffy, B. Transcriptome-level discovery of survival-associated biomarkers and therapy targets in non-small-cell lung cancer. *Br. J. Pharmacol.* **181**, 362–374 (2024).

26. Chandrashekar, D. S. *et al.* UALCAN: A Portal for Facilitating Tumor Subgroup Gene Expression and Survival Analyses. *Neoplasia N. Y. N* **19**, 649–658 (2017).

27. Chandrashekar, D. S. *et al.* UALCAN: An update to the integrated cancer data analysis platform. *Neoplasia N. Y. N* **25**, 18–27 (2022).

28. Wiederschain, D. *et al.* Single-vector inducible lentiviral RNAi system for oncology target validation. *Cell Cycle Georget. Tex* **8**, 498–504 (2009).

29. Huttlin, E. L. *et al.* A tissue-specific atlas of mouse protein phosphorylation and expression. *Cell* **143**, 1174–1189 (2010).

30. Liu, Q., Yin, X., Languino, L. R. & Altieri, D. C. Evaluation of drug combination effect using a Bliss independence dose-response surface model. *Stat. Biopharm. Res.* **10**, 112–122 (2018).

31. Bachmanov, A. A., Reed, D. R., Beauchamp, G. K. & Tordoff, M. G. Food Intake, Water Intake, and Drinking Spout Side Preference of 28 Mouse Strains. *Behav. Genet.* **32**, 435–443 (2002).

32. Cunniff, B., Snider, G. W., Fredette, N., Hondal, R. J. & Heintz, N. H. A direct and continuous assay for the determination of thioredoxin reductase activity in cell lysates. *Anal. Biochem.* **443**, 34–40 (2013).

33. Arnér, E. S. J., Zhong, L. & Holmgren, A. Preparation and assay of mammalian thioredoxin and thioredoxin reductase. in *Methods in Enzymology* vol. 300 226–239 (Academic Press, 1999).

34. Gheorghe, V. & Hart, T. Optimal construction of a functional interaction network from pooled library CRISPR fitness screens. *BMC Bioinformatics* **23**, 510 (2022).

35. Stockwell, B. R. *et al.* Ferroptosis: A Regulated Cell Death Nexus Linking Metabolism, Redox Biology, and Disease. *Cell* **171**, 273–285 (2017).

36. Weïwer, M. *et al.* Development of small-molecule probes that selectively kill cells induced to express mutant *RAS*. *Bioorg. Med. Chem. Lett.* **22**, 1822–1826 (2012).

37. Eaton, J. K. *et al.* Selective covalent targeting of GPX4 using masked nitrile-oxide electrophiles. *Nat. Chem. Biol.* **16**, 497–506 (2020).

38. Cheff, D. M. *et al.* The ferroptosis inducing compounds RSL3 and ML162 are not direct inhibitors of GPX4 but of TXNRD1. *Redox Biol.* **62**, 102703 (2023).

39. Stancill, J. S. & Corbett, J. A. The Role of Thioredoxin/Peroxiredoxin in the β-Cell Defense Against Oxidative Damage. *Front. Endocrinol.* **12**, 718235 (2021).

40. Netto, L. E. S. & Antunes, F. The Roles of Peroxiredoxin and Thioredoxin in Hydrogen Peroxide Sensing and in Signal Transduction. *Mol. Cells* **39**, 65–71 (2016).

41. Huang, F., Han, X., Xiao, X. & Zhou, J. Covalent Warheads Targeting Cysteine Residue: The Promising Approach in Drug Development. *Molecules* **27**, 7728 (2022).

42. Randolph, J. T. *et al.* Discovery of a Potent Chloroacetamide GPX4 Inhibitor with Bioavailability to Enable Target Engagement in Mice, a Potential Tool Compound for Inducing Ferroptosis In Vivo. *J. Med. Chem.* **66**, 3852–3865 (2023).
43. Balfourier, A., Kolosnjaj-Tabi, J., Luciani, N., Carn, F. & Gazeau, F. Gold-based therapy: From past to present. *Proc. Natl. Acad. Sci.* **117**, 22639–22648 (2020).
44. Abdalbari, F. H. & Telleria, C. M. The gold complex auranofin: new perspectives for cancer therapy. *Discov. Oncol.* **12**, 42 (2021).
45. Marzano, C. *et al.* Inhibition of thioredoxin reductase by auranofin induces apoptosis in cisplatin-resistant human ovarian cancer cells. *Free Radic. Biol. Med.* **42**, 872–881 (2007).
46. Fiskus, W. *et al.* Auranofin induces lethal oxidative and endoplasmic reticulum stress and exerts potent preclinical activity against chronic lymphocytic leukemia. *Cancer Res.* **74**, 2520–2532 (2014).
47. Bak, D. W., Gao, J., Wang, C. & Weerapana, E. A Quantitative Chemoproteomic Platform to Monitor Selenocysteine Reactivity within a Complex Proteome. *Cell Chem. Biol.* **25**, 1157-1167.e4 (2018).
48. Radenkovic, F., Holland, O., Vanderlelie, J. J. & Perkins, A. V. Selective inhibition of endogenous antioxidants with Auranofin causes mitochondrial oxidative stress which can be countered by selenium supplementation. *Biochem. Pharmacol.* **146**, 42–52 (2017).
49. Lamarche, J. *et al.* Mass spectrometry insights into interactions of selenoprotein P with auranofin and cisplatin. *J. Anal. At. Spectrom.* **37**, 1010–1022 (2022).

50. Zou, P. *et al.* Auranofin induces apoptosis by ROS-mediated ER stress and mitochondrial dysfunction and displayed synergistic lethality with piperlongumine in gastric cancer. *Oncotarget* **6**, 36505–36521 (2015).

51. Rano, T. A. *et al.* A combinatorial approach for determining protease specificities: Application to interleukin-1β converting enzyme (ICE). *Chem. Biol.* **4**, 149–155 (1997).

52. Schotte, P., Declercq, W., Van Huffel, S., Vandenabeele, P. & Beyaert, R. Non-specific effects of methyl ketone peptide inhibitors of caspases. *FEBS Lett.* **442**, 117–121 (1999).

53. Vandenabeele, P., Galluzzi, L., Vanden Berghe, T. & Kroemer, G. Molecular mechanisms of necroptosis: an ordered cellular explosion. *Nat. Rev. Mol. Cell Biol.* **11**, 700–714 (2010).

54. Blocka, K. L. N., Paulus, H. E. & Furst, D. E. Clinical Pharmacokinetics of Oral and Injectable Gold Compounds. *Clin. Pharmacokinet.* **11**, 133–143 (1986).

55. Kuzell, W. C. Complications of gold therapy and their management. *Calif. Med.* **71**, 140–143 (1949).

56. Capparelli, E. V., Bricker-Ford, R., Rogers, M. J., McKerrow, J. H. & Reed, S. L. Phase I Clinical Trial Results of Auranofin, a Novel Antiparasitic Agent. *Antimicrob. Agents Chemother.* **61**, e01947-16 (2017).

57. Endres, L. *et al.* Alkbh8 Regulates Selenocysteine-Protein Expression to Protect against Reactive Oxygen Species Damage. *PLoS ONE* **10**, e0131335 (2015).

58. Leonardi, A., Evke, S., Lee, M., Melendez, J. A. & Begley, T. J. Epitranscriptomic systems regulate the translation of reactive oxygen species detoxifying and disease linked selenoproteins. *Free Radic. Biol. Med.* **143**, 573–593 (2019).

59. Songe-Møller, L. *et al.* Mammalian ALKBH8 Possesses tRNA Methyltransferase Activity Required for the Biogenesis of Multiple Wobble Uridine Modifications Implicated in Translational Decoding. *Mol. Cell. Biol.* **30**, 1814–1827 (2010).
60. Fu, D. *et al.* Human AlkB homolog ABH8 Is a tRNA methyltransferase required for wobble uridine modification and DNA damage survival. *Mol. Cell. Biol.* **30**, 2449–2459 (2010).
61. Madhwani, K. R. *et al.* tRNA modification enzyme-dependent redox homeostasis regulates synapse formation and memory. *BioRxiv Prepr. Serv. Biol.* 2023.11.14.566895 (2023) doi:10.1101/2023.11.14.566895.
62. Lee, M. Y., Leonardi, A., Begley, T. J. & Melendez, J. A. Loss of epitranscriptomic control of selenocysteine utilization engages senescence and mitochondrial reprogramming. *Redox Biol.* **28**, 101375 (2020).
63. Lee, M. Y. *et al.* Selenoproteins and the senescence-associated epitranscriptome. *Exp. Biol. Med. Maywood NJ* **247**, 2090–2102 (2022).
64. Evke, S., Lin, Q., Melendez, J. A. & Begley, T. J. Epitranscriptomic Reprogramming Is Required to Prevent Stress and Damage from Acetaminophen. *Genes* **13**, 421 (2022).
65. van den Born, E. *et al.* ALKBH8-mediated formation of a novel diastereomeric pair of wobble nucleosides in mammalian tRNA. *Nat. Commun.* **2**, 172 (2011).
66. Maddirevula, S. *et al.* Insight into ALKBH8-related intellectual developmental disability based on the first pathogenic missense variant. *Hum. Genet.* **141**, 209–215 (2022).
67. Saad, A. K. *et al.* Neurodevelopmental disorder in an Egyptian family with a biallelic ALKBH8 variant. *Am. J. Med. Genet. A.* **185**, 1288–1293 (2021).

68. Reich, H. J. & Hondal, R. J. Why Nature Chose Selenium. *ACS Chem. Biol.* **11**, 821–841 (2016).